Passivation of Ni-Cr and Ni-Cr-Mo Alloys in Low and High pH Sulfate Solutions

Katie Lutton, Junsoo Han, Hung M Ha, Debashish Sur, Elena Romanovskaia, John R Scully

Passivation of Ni-Cr and Ni-Cr-Mo Alloys in Low and High pH Sulfate Solutions

Katie Lutton,[1,2] Junsoo Han,[1,2,3] Hung M. Ha,[4] Debashish Sur,[1,2] Elena Romanovskaia,[1,2,*,z] and John R. Scully[1,2,**,z]

[1]Center for Electrochemical Science and Engineering, University of Virginia, Charlottesville, Virginia 22904, USA

[2]Department of Materials Science and Engineering, University of Virginia, Charlottesville, Virginia 22904, USA

[3]Sorbonne Université, Laboratoire Interfaces et Systèmes Electrochimiques, F-75005, Paris, France

[4]Canadian Nuclear Laboratories, Chalk River, ON, Canada K0J 1J0

*Electrochemical Society Member.

** Electrochemical Society Fellow.

[z]E-mail: jrs8d@virginia.edu; ggd2dr@virginia.edu

Abstract

The kinetics of passive oxide film formation, its thickening, and composition on Ni-22Cr and Ni-22Cr-6Mo wt.% alloys were investigated selected anodic potentials. Experiments were performed in acidic and alkaline sulfate environments using a number of characterization techniques including a combination of potentiodynamic polarization, on-line atomic emission spectro-electrochemistry (AESEC), *in situ* potentiostatic passive film growth, along with *in situ* neutron reflectometry (NR) and *ex situ* X-ray photoelectron spectroscopy (XPS). The roles of solution pH and Mo on the passivation behavior were discussed in terms of thermodynamic and kinetic factors governing passivation. The pH was found to have an impact on the relative chemical compositions of passive film of the Ni-22Cr alloy but not noticeably for the Ni-22Cr-6Mo alloy. Ni-rich films formed early during the passivation process while Cr(III) enrichment was observed at longer times albeit less extensively than observed previously in Cl^- solutions. The fraction of Cr(III) cations also increased with alloying of Mo at low and high pH demonstrating a strong effect of Mo on Cr(III) content during aqueous passivation in Ni based superalloys however a larger

effect is seen in Cl^-. This is a noteworthy finding as Mo is usually assumed to mainly influence pit and crevice stabilization.

Introduction

The passivation of pure Ni metal[1–12] and Ni-based alloys[3,9,12–20] in sulfate environments has been studied to understand the formation, dissolution mechanisms, and the stability of the passive film. For Ni, its passive film is often described by a bilayer structure with an inner crystalline NiO and an outer porous, and hydrated $Ni(OH)_2$ layers. This structure is observed on alloys exposed to sulfuric and perchloric acidic, as well as to alkaline solutions with limiting thicknesses measured on the order of a few nanometers[1].

Electrochemical passivation can be greatly improved with the addition of alloying elements. At lower Cr concentrations, the passive film formed is predominantly NiO-based as there is not sufficient Cr present for formation of a continuous film[16,21,22]. Previous work reported that the addition of a few at.% of Cr to Ni altered the preferred oxidation mechanism from one dominated by outward cation diffusion to one where oxygen ingress was substantial[23]. Above approximately 13 at.% Cr, Ni-Cr alloys preferentially form a continuous Cr-rich oxide/hydroxide film because these particular compounds are more thermodynamically stable and also kinetically favored than Ni-rich ones[15,22]. In the case of high temperature oxidation at 700 ^oC, it was observed that NiO formed first, followed by subsurface Cr_2O_3 enrichment at the inner interface and eventually the emergence of large $NiCr_2O_4$ islands[17]. While in general, the addition of Cr to Ni introduces excellent resistance to localized corrosion[24–29] and increases passive film stability in halide-free acidic solutions[18,30], transpassive dissolution is possible for Cr-rich passive films in highly oxidizing environments[27,29]. This can be remediated through alloying with other elements[31–33].

One of the most common alloying elements used in the Ni-Cr system for corrosion resistance improvement is Mo. Addition of Mo to pure Ni metal provides a less significant effect on the passive film structure compared to the effect of Cr. Ni alloyed with 13 wt.% Mo and passivated in 1 N Na_2SO_4 solution acidified to pH 2.8 has been studied using scanning transmission electron microscopy. The electron diffraction results indicated only the presence of crystalline NiO particles with approximately 3 nm diameters. Mo, however, was found to be either finely dispersed in the NiO film or present as an amorphous species that did not appear in the electron diffraction

patterns[9]. While the addition of Cr alone improves the passivity of Ni-based alloys, Mo addition has been argued to impair passivity as evidenced by increases in the passive current density and the film growth rate[24]. A defective, amorphous $(Mo^{+4}, Mo^{+6})_xO_y$ layer was produced which increases the defect concentrations in NiO, accounting for the observed increase in passive current density[25].

Alloying with both Cr and Mo, however, usually results in a highly synergistic relationship with regards to the passivity as seen in both the Fe and Ni-based systems[34]. This effect is especially notable in chloride containing environments but corrosion resistance is similarly improved in acidic sulfate environments. For instance, Alloy 59 (Ni-22.5Cr-15.5Mo-0.9Fe, wt.%) has been studied in sulfuric acid solutions using potentiodynamic polarization, electrochemical impedance spectroscopy (EIS), X-ray photoelectron spectroscopy (XPS), and sputter depth profiling via Auger spectroscopy[26]. The results indicated a substantial increase in the passivity of the material when alloyed with high concentrations of Cr and Mo compared to pure Ni and its binary alloys. Passive films formed in air exhibited (Cr, Ni)-oxide films whereas those formed in solutions were hydrated (Cr, Ni)-hydroxides[26]. Additionally, the air-oxidized films were thicker by approximately a nanometer in sulfuric acid likely due to the competition between film growth and dissolution absent in the case of the air films oxide. The passive film was not found to exhibit a bi-layered or multi-layered structure. Instead, XPS and Auger depth profiling suggested that the aforementioned oxide species were distributed throughout the film with no preferential segregation to the inner or outer interfaces[26]. Additional work has been reported in aggressive sulfuric acid solutions (0.5 M) deaerated by Ar and characterization by Time-of-Flight Secondary Ion Mass Spectrometry (ToF-SIMS) as well as XPS[30,35]. Passivation was achieved in this study at potentials of 0.25 V/SCE and 0.3 V/SCE, for Ni-20Cr and Ni-20Cr-10Mo (wt.%) respectively (by stepping the potential from OCP to the selected potential, and maintaining the polarization for 4 h. The film was found to be enriched in Cr(III) for both alloys, and Mo oxide was suggested to form between the outer/inner layers interface for the Mo-containing alloy[30,35]. At higher potentials, soluble Mo species were formed. Cycles of spontaneous passivation after cathodic reduction supported the continuous accumulation of Mo cations in passive films. In other recent study, the potentiodynamic passivation of Ni-22%Cr and Ni-22%Cr-6%Mo, wt.%, alloys were investigated using elemental resolved polarization curves in aerated and deaerated sulfuric acid solutions[18]. Alloying with Mo

improved the long-term passivity by favoring the formation of Cr_2O_3 in the film, and also resulted in significant Mo accumulation within the oxide. The most recent studies of the passive film growth on the Ni-Cr alloy systems with alloying elements in chloride deaerated solutions were conducted for long periods of exposure up to 10^5 s[31,36] and 10^6 s[37]. These studies showed that Ni(II) formed early, Cr(III) enrichment occurred with time changing the overall oxide film composition. Cr oxides and hydroxides were formed at short passivation times while spinels were detected at longer times[31,36,37]. Mo was incorporated into these oxides. Therefore, while the studies in Cl^- solutions provide information on the influence of Mo on Cr(III) enrichment in the passive film with time, the up-to-date ones in sulfate solutions do not contain such information. However, it is essential to know how the minor alloying elements influence on the growth and the composition of the passive film in sulfate solutions, at both acidic and alkaline pH.

The objective of this study is to revisit the effects of Mo at fixed solution pH on the kinetics of passive film growth on Ni-based alloys over second to 10 ks times frames without the effect of Cl^- on film dissolution. *In operando* film growth is analyzed by atomic emission spectroelectrochemistry (AESEC), and single frequency-electrochemical impedance spectroscopy (SF-EIS) measurements in both acidic and alkaline sulfate environments. The film composition, thickness, and their variations with passivation time during a potentiostatic film growth are characterized using *ex situ* XPS and *in situ* neutron reflectometry (NR). The role of pH on passive film growth is investigated through direct comparison of a mildly acidic (pH 4) solution with a mildly alkaline one (pH 10). The results provide more insights into the role of Mo during acidic and alkaline passive film growth and its synergistic relationship when alloyed with Cr.

Materials and Experiments

The samples used in this study were polycrystalline, solid solution Ni-based alloys with the compositions of Ni-22Cr and Ni-22Cr-6Mo[A] that model common Cr and Mo concentrations in commercial Ni-based superalloys. The materials were arc-melted, cast, rolled, recrystallized at 1100 ^oC for 40 min, quenched, and sectioned[27]. Prior to each experiment, the samples were wet-polished up to 1200 grit using SiC paper, ultrasonically cleaned in ethanol and rinsed with

[A] In this study, Ni-22Cr (wt.%) and Ni-22Cr-6Mo (wt.%) alloys are denoted as Ni-22Cr and Ni-22Cr-6Mo, respectively. For XPS and AESEC calculations the alloys compositions in at. % - Ni-24Cr and Ni-24.7Cr-3.7Mo - were used.

deionized water (Milli-Q, resistivity of 18.2 MΩ-cm) before being placed into the electrochemical cell.

The solutions used in film passivation experiments were 0.1 M Na_2SO_4 adjusted to pH 4 by 1.0 M H_2SO_4, and 0.1 M Na_2SO_4 pH 10 adjusted by 1.0 M NaOH. All solutions were prepared using reagent grade chemicals and deionized water. During electrochemical experiments the solutions were deaerated using N_2 gas.

An initial cathodic reduction step at -1.3 V vs. saturated calomel electrode (SCE) for 10 min was conducted before all electrochemical experiments in order to minimize the effect of air-formed oxides on the alloy surface[28]. Following the cathodic reduction step, potentiodynamic polarization was performed from -1.3 V_{SCE} to +0.8 V_{SCE} with 1 mV/s scan rate, while *in situ* monitoring the imaginary impedance (Z'') at 1 Hz using a 20 mV_{rms} AC signal. Similarly, after a cathodic reduction step, potentiostatic passive film growth experiments were performed using the single frequency EIS method at +0.2 V_{SCE} where the current density and Z'' was monitored at 1 Hz for 10 ks. The oxide thickness (l_{ox}) was estimated at the end of measurement. A full frequency EIS spectrum was acquired from 100 kHz to 1 mHz to obtain the constant phase element exponent (α), via a circuit model fit[28] and correlate $-Z"(t)$ to an oxide thickness, $l_{ox}(t)$[29]. From these results, the oxidation current density, $i_{ox}(t)$, may be calculated as:

$$l_{ox}(t) = \frac{-Z"(t)(2\pi f \varepsilon \varepsilon_o)^{\alpha} A}{\rho_{\delta}^{1-\alpha} \sin\left(\frac{\alpha\pi}{2}\right)[1 + 2.88(1-\alpha)^{2.375}]} \quad \text{Equation 1}$$

$$i_{EC}(t) = i_{ox}(t) + i_{diss}(t) \quad \text{Equation 2}$$

$$i_{ox}(t) = \frac{n\rho_{ox}F}{M_{ox}}\frac{dl_{ox}}{dt} \quad \text{Equation 3}$$

$$\eta = \frac{i_{ox}}{i_{EC}} \quad \text{Equation 4}$$

Here f is the applied frequency, ε is the dielectric constant (30 assumed[38]), ε_o is the vacuum permittivity of free space, A is the exposed sample area, ρ_{δ} is the boundary interfacial resistivity ($450\ \Omega - cm$ assumed[39]), i_{EC} is the total anodic current density, i_{diss} is the total measured dissolution current density, n is the cation valency, ρ_{ox} is the oxide or hydroxide density, F is Faraday's constant, M_{ox} is the oxide molar mass, and η is the oxidation efficiency[29].

The AESEC was used to monitor the elemental dissolution rates during passivation. The detailed principles of this technique are available elsewhere[40,41]. The specimen was vertically placed in a specially designed electrochemical flow cell. The electrolyte containing the cations released from the specimen were transferred to an inductively coupled plasma atomic emission spectrometer (ICP-AES, Ultima Expert™ Horiba Jobin Yvon) for chemical analysis. The elemental concentration of the electrolyte as a function of time, $C_M(t)$, was calculated from the atomic emission intensity with a characteristic wavelength of the element M, $I_\lambda(t)$, as:

$$C_M(t) = \kappa[I_\lambda(t) - I_\lambda^o(t)] \quad \text{Equation 5}$$

where $I_\lambda^\circ(t)$ is the background signal, and κ is the sensitivity factor of M obtained separately from a standard ICP calibration method. The elemental current density ($i_{diss}^M(t)$), equivalent to the elemental dissolution rates, may be calculated as:

$$i_{diss}^M(t) = \frac{zFfC_M(t)}{A\,M_M} \quad \text{Equation 6}$$

where z is the oxidation state, f is the flow rate of the electrolyte (2.8 mL min^{-1}), F is Faraday constant, A is the exposed surface area (0.7 cm^2), and M_M is the atomic mass of M.

Electrochemical control was achieved using a Gamry Reference 600 potentiostat. After the cathodic reduction at - 1.3 V_{SCE} for 10 min[28,42], a potentiostatic step to +0.2 V_{SCE}, was implemented to grow the passive film for up to 10,000 s. This potential is relevant to the long-term open circuit potential of Ni-Cr-Mo alloys in seawater and other natural environments where passivation occurs sometimes punctuated by crevice corrosion[43]. Under this applied potential and at pH 4 and 10, the thermodynamically predominant oxidation states of the metals are Ni^{+2}, Cr^{+3}, and Mo^{+6} [44]. The element-specific current density contributions for the cation species, M^{z+}, released into solution and not retained in the oxide as determined by the AESEC measurements, $i_{diss}^M(t)$, were summed to obtain the total current density for dissolution and cation ejection reactions:

$$i_{diss}(t) = \sum i_{diss}^M(t) \quad \text{Equation 7}$$

The $i_{diss}(t)$ value was then subtracted from the total electrochemically measured DC current density, i_{EC}, to estimate the total oxide formation current density, $i_{ox}\ (t)$ in equation 8:

$$i_{ox}(t) = i_{EC}(t) - i_{diss}(t) \quad \text{Equation 8}$$

In order to evaluate the contribution of a specific element M towards passivation rather than direct cation ejection or film dissolution, the expected element-specific dissolution current density based on congruent alloy dissolution[B] where E_{app} is well above the oxidation potential for each element, $i^{M}_{cong\ diss}(t)$, was estimated:

$$i^{M}_{cong\ diss}(t) = z(at.\%\ M) i_{EC}(t) \quad \text{Equation 9}$$

and the oxidation current density contribution of element M may be obtained as follows:

$$i^{M}_{ox}(t) = i^{M}_{cong\ diss}(t) - i^{M}_{diss}(t) \quad \text{Equation 10}$$

The atomic composition of M cations at the surface, N_M, may be calculated as:

$$N_M = \frac{N_A}{zF} q^{M}_{ox} = \frac{N_A}{zF} \int_0^t i^{M}_{ox}(t) dt \quad \text{Equation 11}$$

$$A_M(t) = \frac{N_M(t)}{\sum N_M(t)} \quad \text{Equation 12}$$

where N_A is Avogadro's number and q^{M}_{ox} is the integrated oxidation charge for element M. It is recognized that this estimated cation composition does not account for potential layering nor say anything about the type of oxide or hydroxide formed just the moles oxidized but not dissolved and solubilized per unit area. Equation 12 gives the cation fraction again with no consideration of phase separation or solute capture (in other words the structure and layering cannot be determined). This was used to estimate the oxidized cation fraction that joined the surface layer over 10 ks as a comparison to XPS and NR.

The changes in film composition and thickness was characterized by *ex situ* XPS using PHI VersaProbe III instrument. The spectra were obtained for native air oxides, and periodically after 10 min of cathodic reduction at -1.3 V_{SCE} and potentiostatic passive film growth of 100s, 1000s and 10 ks at +0.2 V_{SCE}. This technique has been well-established for the analysis of the identity, concentration, and thicknesses of individual compounds present in surface thin films[45], especially for the case of Ni-based alloys[28,46,47]. All XPS spectra were obtained using a monochromatic Al-Kα photon source (E = 1,486.7 eV). The take-off angles between the sample

[B] Congruent dissolution is a starting point and a reasonable assumption when there are large thermodynamic driving forces for dissolution of each alloying element, i.e. $i_{diss} \gg i_{ox}$.

and detector were adjusted to 45 and 90°, whereas that between the detector and the X-ray source was fixed at 54.7° (Figure 1). The instrument was calibrated to the $4f_{7/2}$ binding energy (E = 84 eV) of a metallic Au reference measured at the same time. Survey spectra were recorded on all samples using a pass energy of 200 eV, followed by high resolution analysis of the Ni 2p, Cr 3p, Mo 3d, and O 1s regions using a pass energy of 20 eV. No charge neutralization system was employed. The samples were in the electrical contact with the stage.

Commercial CasaXPS software was used to perform Shirley background corrections and spectra fitting based on the peaks and parameters for the expected oxide species[48–50]. The charge correction was done by shifting the C 1s peak binding energy to 284.8 eV, and then shifting all other peaks to the same number of eV. The concentrations of Ni(II), Cr(III), and Mo(IV,VI) species in the passive films were computed by fitting the spectra to their observed metallic and oxide/hydroxide peaks, as established in previous literature[46,47,50–53] and correcting these integrated peak areas to atomic sensitivity factors for Ni, Cr, and Mo (4.044, 2.427, and 3.321 for this detector and source configuration, respectively)[50] (Appendix A).

The calculation of XPS enrichment/depletion factor $f_{(Cr(III))}$ in passive film was accomplished using equation[54]:

$$f_A = \frac{A^{n+}/(A^{n+} + B^{m+} + C^{l+})}{A/(A+B+C)} \qquad \text{Equation 13}$$

where A^{n+}, B^{m+}, C^{l+} – the cationic fraction of the element in the oxide; A, B, C – the atomic fraction of the element in the alloy.

The molecular identity and the layering of passive films were also analyzed using *in situ* neutron reflectometry. The experiments were conducted at the D3 beamline at the National Research Universal (NRU) reactor (Chalk River, Ontario, Canada), shown schematically in Figure B1 (Appendix B). This setup allowed NR measurements to be performed concurrently with electrochemical experiments[C]. Thin film samples for NR experiments were prepared by a sputter deposition system (Plasmionique Inc., Quebec, Canada) to produce approximate 25 nm thick Ni-Cr and Ni-Cr-Mo alloys on 100 mm diameter x 6 mm thick polished Si (111) wafers. XPS analysis following thin film preparation yielded bulk compositions of Ni-20Cr and Ni-20Cr-10Mo. The

[C] Because of the unfortunate shutdown of the D3 neutron beam line, *in situ* passivation measurements were only performed for 0.1 M Na_2SO_4 acidified to pH 4.

thin film samples for NR experiments were stored in a vacuum desiccator and, prior to experiments, were cleaned with methanol and dried in air.

A conventional three-electrode electrochemical cell with a Pt thin foil counter electrode and a KCl saturated Ag/AgCl reference electrode ($V_{Ag/AgCl}$ = +47 mV_{SCE}) was used. The electrochemical experiments were conducted under a Solartron 1287A potentiostat control. Similarly, to all mentioned above electrochemical experiments, the cathodic potential of -1.3 V_{SCE} was applied for 5 min[D]. Then potentiostatic polarization from was performed from -0.8 V_{SCE} to +0.2 V_{SCE} (potentials were adjusted to SCE values for better data comparability) with 0.2 V steps every 6 hours (Figure B2, Appendix B). The NR measurements started 1 hour after the applied potential was switched to the set value and each measurement took approximately 90 min to complete. At least two measurements were performed in each potential step to ensure a steady-state was achieved before moving to the next applied potential. The D3 neutron beam characteristics could be found in[29] and Appendix B.

For analysis of the passive film composition and thickness, the SLD profiles of the unoxidized alloys deposited on Si, and of H_2O exposed to vacuum were simulated using GenX software with the interfacial roughness and SLD values of each layers obtained from experiments (Figure 2)[55]. The SLD for the simulated base metals and electrolyte were then subtracted from the experimental SLD profiles, as indicated in Figure 2, in order to extract the SLD versus depth data for only the passive films.

Results

Electrochemistry of Ni-Alloys in Aqueous Sulfate Environments

The E-log(i) and $-Z''$ vs E curves of Ni-22Cr and Ni-22Cr-6Mo in the acidic and alkaline solutions of interest were established in Figure 3(a) & 3(b), respectively. The oxide thickness was estimated from $-Z''$ using Equation 1 and the results were plotted in the same graph as the impedance data (Figure 3(b)). In both solutions, the alloys exhibited a large passive range extending from the corrosion potential to above +0.5 V_{SCE} (Figure 3(a)). In addition, Ni-22Cr-6Mo exhibited lower passive current density than Ni-22Cr indicating the beneficial effect of Mo addition to the Ni-Cr system (Figure 3(a)).

[D] A shorter time was used for the cathodic reduction for the NR experiments in order to minimize possible damage to the thin film sample caused by H_2 evolution.

The difference in passivity of Ni-22Cr and Ni-22Cr-6Mo near +0.2 V_{SCE} is evident in the alkaline environment. At small anodic overpotentials (e.g., from -0.5 to 0 V_{SCE}), a lower passive current density and a thicker oxide (or passive layer with different dielectric constant) according to the impedance results were observed for the Mo-containing alloy which could be attributed to the effect of the minor solute on inhibiting dissolution. In addition, the films formed on the same alloy during cyclic polarization were, in general, thicker in the acidic environment compared to those formed in the alkaline. The characteristic thickening and thinning rates of each alloy (i.e., the slopes of the oxide thickness vs. E curves in Figure 3(b)) were similar and were consistent with passivity theory positing a few nm/V, with notably Ni-Cr film dissolution initiating at a lower potential and occurring more rapidly than Ni-Cr-Mo alloy in the acidic environment. This is due to a known electrochemical stabilization benefit of Mo[44].

SF-EIS Application to Ni-alloys over a range of pH levels

Potentiostatic passivation of Ni-22Cr and Ni-22Cr-6Mo at +0.2 V_{SCE} in acidic (pH 4) and alkaline (pH 10) 0.1 M Na_2SO_4 was monitored using SF-EIS to investigate the formation of passive film. The $-Z''(t)$ as a function of time in the acidic environment for Ni-22Cr and Ni-22Cr-6Mo obtained from the SF-EIS measurements at 1 Hz and +0.2 V_{SCE} are shown in Figure 4. The $-Z''(t)$ and the corresponding $l_{ox}(t)$, calculated from Equation 1, (assuming a Cr rich passive film) were slightly smaller in alloys containing Mo. This can be seen in both the early stage of passive film formation (i.e., a few seconds after potentiostatic experiment) and at longer periods during film formation (i.e., above 1000 s). In addition, the passive film thickness did not change much after approximately 1000 s for both Mo-free and Mo-containing alloys.

The passivation-time behavior of Ni-22Cr and Ni-22Cr-6Mo in 0.1 M Na_2SO_4 solution adjusted to various pH values are shown in Figures 6a and 6b, respectively. It can be seen that at all pH levels i_{ox} is below i_{EC} and η is less than 1 even in the most alkaline solution. At early passivation times such as 10–100 s efficiency increases with increasing pH. At later times such as 1ks–10ks, efficiency approaches very low levels as the passive current density maintains a nearly constant passive film thickness. The film thickness estimated by SF-EIS on both Ni-22Cr and Ni-22Cr-6Mo increases with pH (Figure 5), likely due to the chemical stability of certain hydroxides or oxides. This was confirmed through the analysis of the oxidation rate, i_{ox}, and the efficiency, η

(Equation 4), for the alloys, shown in Figure 6. As predicted by the faster passivation with increasing pH values, η generally increases for each alloy.

AESEC passivation of Nickel Alloys in 0.1 M Na_2SO_4

The equivalent elemental dissolution current densities, i_{diss}^{M}, determined using Equation 6 for the Ni-22Cr (Figure 7(a)) and Ni-22Cr-6Mo (Figure 7(b)) alloys in 0.1 M Na_2SO_4 pH 4 solution are shown by solid lines with a comparison to the partial electrochemical current densities for each elements ($i_{cong\ diss}^{M}$) calculated using Equation 9. The differences between the i_{diss} versus time for each element (i_{diss}^{Ni}, i_{diss}^{Cr}, i_{diss}^{Mo}) and the corresponding $i_{cong\ diss}^{M}$ indicates the elemental contributions to the non-dissolved oxidized species accumulating on the surface in some manner. It should be noted that the i_{EC} for the AESEC figures were convoluted, taking into account the residence time distribution of the elemental dissolution signal in the flow cell[41].

The low values of i_{diss} compared to i_{EC} indicates that there is a higher efficiency but less than 1 for oxide growth versus dissolution at early stage of passivation. However, a significant role of cation ejection during passivation in acidic sulfate solutions is evident. In the case of the Ni-22Cr, the AESEC data shown in Figure 7(a) indicates that there were non-dissolved oxidized Ni-species present for the initial stage of passivation, followed by later enrichment of a passive, Cr-rich oxide film.

The Ni-22Cr-6Mo shown in Figure 7(b) has similar initial Ni(II) formation accumulating on the surface over the first 10 s followed by Ni(II) mostly dissolving when oxidized during subsequent Cr-enrichment of the passive film. A gradual decrease in i_{diss}^{Ni}, nearly matches i_{EC} whereas i_{diss}^{Cr}, and i_{diss}^{Mo}, remain below i_{EC} at all times indicating that these cations accumulate on the surface or join the passive film. At longer times, a quasi-limiting thickness is attained (Figure 5(b)) and dissolution observed using AESEC corresponds to ejection of the alloying elements from the passive film and oxidation of elements to maintain the thickness in Figure 5. The gradual enrichment of Cr(III) accumulated continually occurs after 100 s, as shown in Figure 8(a), presumably as a result of favorable oxide film formation with Mo-alloying[56]. The i_{diss}^{Mo} indicates that, after early Mo release during Cr-film enrichment, it likely becomes incorporated in the oxide at small concentrations.

Elemental dissolution rates of Ni-22Cr and Ni-22Cr-6Mo in the alkaline media, 0.1 M Na_2SO_4 pH 10, were under the detection limits, therefore, are not presented herein. The cation concentrations at the surface given in Figure 8(b) were approximated using the base metal alloying content.

Neutron Reflectometry of Nickel Alloys

The reflectivity curves for the two alloys in 0.1 M Na_2SO_4 pH 4 are given in Figure 9. These data sets were fitted using an algorithm developed by Parratt[55,57–59] to produce neutron SLD profiles versus depth (Figure 10). The reflectivity curves were best fitted using a passive film model comprised of a single-phase inner oxide layer and an outer hydroxide layer rather than a model comprised of separated inner oxide layers of NiO and Cr_2O_3 and an outer hydroxide layer. At low depths, the SLDs were close to -0.5×10^{-6} Å^2 corresponding to the electrolyte layer. At greater depths (i.e., between approximately 50 and 110 Å in Figure 10(a) and between approximately 150 and 270 Å in Figure 10(b)), the SLDs gradually increased to ca. 1.5×10^{-6} Å^2, corresponding to the outer hydrated oxide layer. A steep increase in the SLD at higher depths (i.e., between approximately 110 and 130 Å in Figure 10(a) and between approximately 270 and 290 Å in Figure 10(b)) corresponded to the interface between the outer hydrated oxide layer and the inner oxide layer of the passive film. The humps in the SLD profiles at the depth between ca. 130 and 160 Å in Figure 10(a) and between ca. 290 and 320 Å in Figure 10(b) corresponded to the inner oxide layers. Finally, the SLD of the base metal alloys was reached at greater depths. Annotated on Figure 10 as horizontal lines are the theoretical SLD of several stoichiometric oxides and hydroxides. SLD values of the inner oxide layers formed on the two alloys suggest the layers were rich in Ni-oxide species.

Simulated SLD profiles for a non-equilibrium film with varying Cr(III) content were produced using GenX software (Figure 11). One notable change in the SLD profiles of a non-equilibrium film with varying Cr(III) is that when the content of Cr(III) increased, the SLD of the oxide layer gradually decreased until it reached the theoretical SLD value of Cr_2O_3.

The SLD profiles of the stand-alone passive film after subtraction of the metal and electrolyte SLDs (Figure 2) are shown in Figure 12. These results additionally allow for the estimation of l_{ox} and the Cr(III) cation fraction using the width and height of the profile, respectively. Films with an SLD closer to the theoretical SLD value of NiO (8.7×10^{-6} A^{-2}) will

have a lower % Cr(III) compared to those near the theoretical SLD value of Cr_2O_3 (5.1×10^{-6} A^{-2}), and the non-stoichiometric film possessing an SLD in-between the two. The SLDs of the inner layer on both alloys were close to the theoretical SLD value of NiO suggesting the oxide films on both alloys were rich in Ni, similar to previous work[46,60,61]. For Ni-Cr-Mo, the SLD of the outer layer decreased with increased potential suggesting a selective dissolution of Ni(II) in favor of Cr-enrichment as the potential increased (Figure 12(b)). The small SLD of the outer layer is attributed to a highly hydrated nature of the layer. The thickness of the outer layer was estimated to be several nm from the SLD profiles.

Analysis of the Cr(III) metal cation fraction and the passive film thickness was conducted using the profile width and peak SLD values in Figure 12. The Ni-Cr-Mo alloy exhibited greater Cr-enrichment in the oxide film than the Ni-Cr alloy across all potentials (Figure 13(a)). The film thickness was also consistently greater on the Ni-Cr-Mo alloy at every potential investigated in this work, suggesting the effect of Mo on promoting Cr-oxidation and passive film formation (Figure 13(b)). There is small variation in both Cr(III) cation fraction and film thickness with applied potentials due to relatively slow dissolution kinetics in sulfate environments. The slight thinning of the film at higher potentials can be attributed to the transpassive oxide dissolution. At higher potentials (e.g. +550 mV_{SCE})[44], fast transpassive dissolution of Cr(III) would result in more noticeable thinning[62].

XPS Analysis of Nickel Alloys

An example of the deconvolution of the XPS spectra for the Ni-Cr-Mo alloy passivated at +0.2 V_{SCE} for 10 ks after 600 s of cathodic potential step at -1.3 V_{SCE} in 0.1 M Na_2SO_4 pH 4 is shown in Figure 14. The fitted peaks are consistent with the presence of $Ni(OH)_2$, NiO, $Cr(OH)_3$, Cr_2O_3, MoO_2, and MoO_3 in the passive film but contain no structural verification. It should be noted that previous literature has additionally identified spinel compounds (e.g. $NiCr_2O_4$)[16,17,63–65], but it was found that during peak fitting these phases only constituted an insignificant fraction (≤ 1%) of the total integrated area and as such were excluded from the current analysis.

The comparison of the XPS fitted data of native-formed oxide film (Figure 8(a) & (b)) and that of the film after cathodic reduction (Table 1) showed a slight higher cation fraction of Cr(III) for Ni-22Cr alloy after cathodic reduction step at -1.3V_{SCE} in both acidic and alkali solutions but only for Ni-22Cr-6Mo in acidic solution. At the same time, the composition of the film on Ni-

22Cr-6Mo after cathodic reduction in 0.1 Na_2SO_4 pH10 solution remained close to the native-formed oxide. It must be mentioned that the thickness of the film after the cathodic reduction step was much lower (according to a comparison of the intensity of metal and metal oxides/hydroxides peaks), and the composition of the film underlying alloy layer remained almost unchanged.

The XPS enrichment/depletion factor $f_{Cr(III)}$ in passive film calculated by equation 13[54] (Figure 15) shows that at pH 4, the Ni-22Cr alloy (Figure C1, Appendix C) exhibited lower enrichment of Cr-species in its passive film than Ni-22Cr-6Mo (Figure C2, Appendix C), resulting in a higher cation fraction of Cr(III) in the passive film when Mo was alloyed. Upon comparing passivation in an acidic environment (Figure 8(a)) to that in an alkaline one (Figure 8(b)), there is an apparent difference in the composition between the films. The fraction of Ni(II) measured using XPS peak fitting and AESEC analysis remained steady for the Ni-22Cr alloy, whereas there was slight but statistically significant enrichment of Cr(III) within the film on the Ni-22Cr-6Mo alloy throughout the passivation time (Figure 15). For all times, there was additionally a slightly greater fraction of Cr(III) within the film on the Ni-22Cr-6Mo alloy than on the Ni-22Cr alloy after 10 ks (Figure 8(a)). Finally, the calculated cation fractions of Mo(IV,VI) in the passive film were lower for pH 10 (Figure 8(b)) than that observed at pH 4 (Figure 8(a)) probably due to MoO_3^{2-} stability at high pH.

In the alkaline environment, the measured Ni $2p^{3/2}$ spectra were predominantly representative of Ni metal and $Ni(OH)_2$ (Figures C3 and C4, Appendix C) and Cr metal and $Cr(OH)_3$ for the Cr $2p_{3/2}$ spectra. Spectral fitting suggests there were some oxide species present at all times in the acidic environment because of its favorable thermodynamics over the hydroxides, whereas both were stable at pH 10 and the oxides became hydrated $Ni(OH)_2$ and $Cr(OH)_3$. Less Mo(IV,VI) was found within the alkaline passive film. This can be attributed to its poor thermodynamic stability in high pH environments[44].

Following the 10 ks passivation, the films formed on Ni-22Cr and Ni-22Cr-6Mo in both the acidic and alkaline environments were analyzed using an XPS take-off angles of 45° and 90° (Figure C5 to Figure C7, Appendix C). The spectra are normalized to the intensity of the metal peaks to demonstrate the increased sensitivity for the surface chemistry and suggest any preferential outer environment of certain oxide species. The spectra were representative of the same oxide/hydroxide species. Spectral fitting, however, demonstrated that there was slight

enrichment of Ni(II) species and depletion of Cr(III) at the film/solution interface following passivation in the alkaline environment for both Ni-Cr and Ni-Cr-Mo (Figure 16). Notably, Mo(IV,VI) was not affected by the preferential Ni(II) surface enrichment and appears to be present at a similar concentration throughout the film. No clear surface enrichment was observed for the films formed in the acidic environment.

Discussion

Passive film formation is rapid during single step passivation and efficiency lower than 100% for Ni(II), Cr(III) and Mo(IV, IV). For every nanometer of oxide formed, 0.5 nm of metal is dissolved at 100% efficiency. The results strongly suggest an early pre-dominance by hydroxylated NiO or $Ni(OH)_2$, possibly containing solute captured Cr(III), followed by very slow enrichment of Cr(III) within the passive film during single step passivation. Evidence of solute capture are suggested by initial oxide cation fractions very close to the alloy element fractions and the slow dissolution rate of Ni in sulfate at pH 10 relative to Cl^- where Cr(III) enrichment is faster. During single step passivation a pseudo steady state is reached after 1000 s[66] and in pH 10 sulfate remain rich in Ni(II). Alloying with Mo supports some later and gradual preferential oxidation of Cr to Cr(III) within the film, resulting in Ni(II) cation ejection. Mo, when included as a minor alloying element, becomes incorporated into the passive film in low concentrations.

The results performed in the mildly acidic (pH 4) and mildly alkaline (pH 10) sulfate environments demonstrate different characteristics of the passive films formed in each environment. Less preferential Ni-dissolution and subsequent Cr-enrichment was observed in the alkaline environment, probably due to the increased thermodynamic stability of these oxides and the lower solubility of $NiSO_4$ compared to $NiCl_2$[67] (Figure 8(b)). This is supported by Pourbaix's predictions[44], where NiO and $Ni(OH)_2$ are thermodynamically stable at pH > 5. The lack of significant Cr enrichment in the passive films compared to previous studies performed in chloride environments[29] demonstrates the influence of preferential dissolution of Ni(II) on the evolution of passive film compositions. Passivation in a sulfate environment still supports the previous theory[66] that Mo alloying promotes the oxidation of Cr. The calculated enrichment of Mo(IV,VI) cations was lower for pH 10 (Figure 8(b)) than that observed at pH 4 (Figure 8(a)), due to its thermodynamic instability and likely selective dissolution in the alkaline environment as MoO_4^{2-}.

The passive films formed in the acidic sulfate environment exhibited a distribution of cations that suggests nonequilibrium solute capture (Figure 11(a)), where a mixed oxide is speculated (e.g. $Ni_{1-x}Cr_xO_y$) was observed instead of the traditionally expected, phase-distinct, bilayer structure (e.g. NiO/Cr_2O_3/Ni-Cr(-Mo)) (Figure 11(b)). For the film formed in the alkaline sulfate environment, however, angle-resolved XPS exhibited some outer enrichment of predominantly NiO (Figure 16). The difference was, albeit, slight but the stability of Ni(II) in the film resulted in some segregation to the film/solution interface. Interestingly, Mo was not observed to vary in composition throughout the film formed in either environment as a result of solute capture. Due to the low concentration within the alloy, no segregation was observed.

The passive dissolution rate and breakdown of the oxide are often attributed to and rates regulated by the features and properties of the passive film. It is clear that the passive films of Ni-Cr-X alloys take on many forms depending of exposure conditions and aging (exposure time). Caution is therefore warranted in assigning corrosion properties under any one condition given a that a large variety of passive film characteristics can be realized depending on anion (i.e., Cl^- vs sulfate), pH, growth rate and potential, exposure aging time. These variable need to be precisely controlled in order to produce a particular passive film which then governs the electrochemical corrosion properties likely in many cases to rely heavily on the exact make-up of the oxide.

Conclusions

The passivation and dissolution of Ni-22Cr and Ni-22Cr-6Mo (wt.%) alloys, were investigated in both acidic and alkaline Na_2SO_4 environments under potentiostatic conditions using *in operando* AESEC and SF-EIS, *in situ* NR, and *ex situ* XPS. The combination of the AESEC technique may enable determination of i_{ox} distinctly from i_{EC} with high temporal resolution. It was determined that Ni-rich films form early during the passivation process, indicating the substantial influence of kinetic factors. At longer times, Cr(III) enrichment was observed when thermodynamics predominated the film composition. Surface films formed during potentiostatic polarization at +0.2 V_{SCE} were consistent with non-stoichiometric solid solution rock salt and corundum oxide structures, likely containing solute captured Ni(II), Cr(III), and Mo(IV,VI) cations. No substantial layering was observed during oxide formation, with the films instead being Ni-rich at the film/electrolyte and Cr-rich at the metal/film interfaces. Oxides were first formed, with compositions governed by non-equilibrium solute capture. The electrochemical stability of

Cr(III) cations also increased with alloying of Mo in the base metal, noted by the respective dissolution currents being measured below the detection limit for the Ni-22Cr-6Mo alloy in each environment. Surface films formed during anodic polarization in the alkaline environment were found to be enriched in Ni(II) cations because of the increased stability of NiO and $Ni(OH)_2$.

Acknowledgements

KL, ER, and JRS acknowledge support from ONR MURI "Understanding Atomic Scale Structure in Four Dimensions to Design and Control Corrosion Resistant Alloys" on Grant # N00014-16-1-2280 under the directorship of Dr. Dave Shifler. PHI VersaProbe III system was supported by NSF Award 162601, MRI Acquisition of an X-Ray Photoelectron Spectrometer for Chemical Mapping of Evolving Surfaces: A Regional Instrument for Research and Teaching. The AESEC experiments conducted by JH were supported by the Agence Nationale de Recherche, grant # ANR-20-CE08-0031 (TAPAS 2020).

References

1. Zuili, D., Maurice, V. & Marcus, P. Surface Structure of Nickel in Acid Solution Studied by In Situ Scanning Tunneling Microscopy. *Journal of The Electrochemical Society* **147**, 1393–1400 (2000).
2. MacDougall, B. & Cohen, M. Breakdown of Oxide Films on Nickel. *J. Electrochem. Soc.* **124**, 1185 (1977).
3. Oblonsky, L. J. & Ryan, M. P. In situ XANES study on the active and transpassive dissolution of Ni and Ni-Cr alloys in 0.1 M H_2SO_4. *Journal of The Electrochemical Society* **148**, B405–B411 (2001).
4. Sato, N. & Okamoto, G. A Mechanism of the Anodic Passivation of Nickel in Acid Solution –Higher Valence Oxide Film Theory–. *Transactions of the Japan Institute of Metals* **2**, 113–119 (1961).

5. Sato, N. & Okamoto, G. Anodic Passivation of Nickel in Sulfuric Acid Solutions. *J. Electrochem. Soc.* **110**, 605 (1963).
6. MacDougall, B. & Cohen, M. Mechanism of the Anodic Oxidation of Nickel. *J. Electrochem. Soc.* **123**, 1783 (1976).
7. Scherer, J., Ocko, B. M. & Magnussen, O. M. Structure, dissolution, and passivation of Ni(111) electrodes in sulfuric acid solution: an in situ STM, X-ray scattering, and electrochemical study. *Electrochimica Acta* **48**, 1169–1191 (2003).
8. Iida, M. & Ohtsuka, T. Ellipsometry of passive oxide films on nickel in acidic sulfate solution. *Corrosion Science* **49**, 1408–1419 (2007).
9. Moriya, M. & Ives, M. B. The Structure of Anodic Films Formed on Nickel and Nickel-13 w/o Molybdenum Alloy in pH 2.8 Sodium Sulfate Solution. *Corrosion* **40**, 62–72 (1984).
10. MacDougall, B., Mitchell, D. F. & Graham, M. J. Changes in Oxide Films on Nickel during Long-Term Passivation. *J. Electrochem. Soc.* **132**, 2895 (1985).
11. Hoppe, H.-W. & Strehblow, H.-H. XPS and UPS examinations of the formation of passive layers on Ni in 1 M sodium hydroxide and 0.5 M sulphuric acid. *Surface and Interface Analysis* **14**, 121–131 (1989).
12. Hoppe, H.-W. & Strehblow, H.-H. XPS and UPS examinations of passive layers on Ni and FE53Ni alloys. *Corrosion Science* **31**, 167–177 (1990).
13. Inc., T. I. N. C. *The Corrosion Resistance of Nickel-Containing Alloys in Sulfuric Acid and Related Compounds*. (1983).
14. Ter-Ovanessian, B., Mary, N. & Normand, B. Passivity Breakdown of Ni-Cr Alloys: From Anions Interactions to Stable Pits Growth. *Journal of The Electrochemical Society* **163**, C410–C419 (2016).

15. Lutton, K., Gusieva, K., Ott, N., Birbilis, N. & Scully, J. R. Understanding multi-element alloy passivation in acidic solutions using operando methods. *Electrochemistry Communications* **80**, 44–47 (2017).
16. Luo, L. *et al.* In situ atomic scale visualization of surface kinetics driven dynamics of oxide growth on a Ni–Cr surface. *Chem. Commun.* **52**, 3300–3303 (2016).
17. Luo, L. *et al.* In-situ transmission electron microscopy study of surface oxidation for Ni-10Cr and Ni-20Cr alloys. *Scripta Materialia* **114**, 129–132 (2016).
18. Li, X. *et al.* The contribution of Cr and Mo to the passivation of Ni22Cr and Ni22Cr10Mo alloys in sulfuric acid. *Corrosion Science* **176**, (2020).
19. Jabs, T., Borthen, P. & Strehblow, H.-H. X-Ray Photoelectron Spectroscopic Examinations of Electrochemically Formed Passive Layers on Ni-Cr Alloys. *J. Electrochem. Soc.* **144**, 1231 (1997).
20. Bond, A. P. & Uhlig, H. H. Corrosion Behavior and Passivity of Nickel-Chromium and Cobalt-Chromium Alloys. *J. Electrochem. Soc.* **107**, 488 (1960).
21. McCafferty, E. Oxide networks, graph theory, and the passivity of Ni-Cr-Mo ternary alloys. *Corrosion Science* **50**, 3622–3628 (2008).
22. McCafferty, E. Graph theory and the passivity of binary alloys. *Corrosion Science* **42**, 1993–2011 (2000).
23. Kim, C. K. & Hobbs, L. W. Identification of diffusing species and the dynamic nature of diffusion paths during oxidation of a dilute Ni-Cr alloy. *Oxid Met* **47**, 69–89 (1997).
24. Frankenthal, R. P., Kruger, J., Tachibana, K. & Ives, M. B. Passivity of Metals. in *Proceedings of the Fourth International Symposium on Passivity* (eds. Frankenthal, R. P. & Kruger, J.) vol. 85 878 (The Electrochemical Society, Inc., 1978).

25. Mitrovic-Spepanovic, V. & Ires, M. B. The Nature of Anodic Films on Nickel and Single Phase Nickel-Molybdenum Alloys. *J. Electrochem. Soc.* **127**, 1903–1908 (1980).
26. Luo, H., Gao, S., Dong, C. & Li, X. Characterization of electrochemical and passive behaviour of Alloy 59 in acid solution. *Electrochimica Acta* **135**, 412–419 (2014).
27. Gusieva, K. *et al.* Repassivation Behavior of Individual Grain Facets on Dilute Ni–Cr and Ni–Cr–Mo Alloys in Acidified Chloride Solution. *The Journal of Physical Chemistry C* **122**, 19499–19513 (2018).
28. Jakupi, P., Zagidulin, D., Noël, J. J. & Shoesmith, D. W. The impedance properties of the oxide film on the Ni-Cr-Mo Alloy-22 in neutral concentrated sodium chloride solution. *Electrochimica Acta* **56**, 6251–6259 (2011).
29. Lutton Cwalina, K. *et al.* In Operando Analysis of Passive Film Growth on Ni-Cr and Ni-Cr-Mo Alloys in Chloride Solutions. *Journal of the Electrochemical Society* **166**, C3241–C3253 (2019).
30. Wang, Z. *et al.* Thermal stability of surface oxides on nickel alloys (NiCr and NiCrMo) investigated by XPS and ToF-SIMS. *Applied Surface Science* **576**, 151836 (2022).
31. Gerard, A. Y. *et al.* The role of chromium content in aqueous passivation of a non-equiatomic Ni38Fe20CrxMn21-0.5xCo21-0.5x multi-principal element alloy (x = 22, 14, 10, 6 at%) in acidic chloride solution. *Acta Materialia* **245**, 118607 (2023).
32. Gerard, A. Y., Lutton, K., Lucente, A., Frankel, G. S. & Scully, J. R. Progress in Understanding the Origins of Excellent Corrosion Resistance in Metallic Alloys: From Binary Polycrystalline Alloys to Metallic Glasses and High Entropy Alloys. *Corrosion* **76**, 485–499 (2020).
33. Scully, J. R. *et al.* Controlling the corrosion resistance of multi-principal element alloys. *Scripta Materialia* **188**, 96–101 (2020).

34. McCafferty, E. *Introduction to Corrosion Science*. (Springer Science & Business Media, 2010).

35. Wang, Z. *et al.* XPS and ToF-SIMS Investigation of Native Oxides and Passive Films Formed on Nickel Alloys Containing Chromium and Molybdenum. *J. Electrochem. Soc.* **168**, 041503 (2021).

36. Scully, J. R., Romanovskaia, E., Lutton, K., Gerard, A. Y. & Inman, S. B. Exposure Aging of Passive Films on Multi-Principal Element Alloys and Ramifications Towards Local Corrosion Resistance. *Meet. Abstr.* **MA2022-02**, 733 (2022).

37. Romanovskaia, E., Lutton, K., Amalraj, M., Marks, L. & Scully, J. R. Formation and Long-Time Exposure Aging of Oxides on Ni-Cr and Ni-Cr-X (Mo, W) Alloys in Acidic Chloride Solutions: Ramifications Towards Local Corrosion Resistance. *Meet. Abstr.* **MA2022-02**, 711 (2022).

38. Macdonald, D. D., Sun, A., Priyantha, N. & Jayaweera, P. An electrochemical impedance study of Alloy-22 in NaCl brine at elevated temperature: II. Reaction mechanism analysis. *Journal of Electroanalytical Chemistry* **572**, 421–431 (2004).

39. Chen, Y.-M., Rudawski, N. G., Lambers, E. & Orazem, M. E. Application of Impedance Spectroscopy and Surface Analysis to Obtain Oxide Film Thickness. *J. Electrochem. Soc.* **164**, C563 (2017).

40. Ogle, K. Atomic emission spectroelectrochemistry: Real-time rate measurements of dissolution, corrosion, and passivation. *Corrosion* **75**, 1398–1419 (2019).

41. Ogle, K. & Weber, S. Anodic Dissolution of 304 Stainless Steel Using Atomic Emission Spectroelectrochemistry. *Journal of The Electrochemical Society* **147**, 1770–1780 (2000).

42. Sato, N. Anodic breakdown of passive films on metals. *Journal of The Electrochemical Society* **129**, 255–260 (1982).
43. Lillard, R. S., Jurinski, M. P. & Scully, J. R. Crevice Corrosion of Alloy 625 in Chlorinated ASTM Artificial Ocean Water. *Corrosion* **50**, 251–265 (1994).
44. Pourbaix, Marcel. *Atlas of electrochemical equilibria in aqueous solutions*. (National Association of Corrosion Engineers, 1974).
45. Strohmeier, B. R. An ESCA method for determining the oxide thickness on aluminum alloys. *Surface and Interface Analysis* **15**, 51–56 (1990).
46. Lloyd, A. C., Noël, J. J., McIntyre, S. & Shoesmith, D. W. Cr, Mo and W alloying additions in Ni and their effect on passivity. *Electrochimica Acta* **49**, 3015–3027 (2004).
47. Lloyd, A. C., Noël, J. J., McIntyre, N. S. & Shoesmith, D. W. The open-circuit ennoblement of alloy C-22 and other Ni-Cr-Mo alloys. *JOM* **57**, 31–35 (2005).
48. Biesinger, M. C. *et al.* Resolving surface chemical states in XPS analysis of first row transition metals, oxides and hydroxides: Cr, Mn, Fe, Co and Ni. *Applied Surface Science* **257**, 2717–2730 (2011).
49. Werfel, F. & Minni, E. Photoemission study of the electronic structure of Mo and Mo oxides. *Journal of Physics C: Solid State Physics* **16**, 6091–6100 (1983).
50. Moulder, J. F., Stickle, W. F., Sobol, P. E. & Bomben, K. D. Handbook of X-ray Photoelectron Spectroscopy. 261 (1992).
51. Biesinger, M. C., Payne, B. P., Lau, L. W. M., Gerson, A. & Smart, R. S. C. X-ray photoelectron spectroscopic chemical state Quantification of mixed nickel metal, oxide and hydroxide systems. *Surface and Interface Analysis* **41**, 324–332 (2009).

52. Biesinger, M. C. *et al.* Quantitative chemical state XPS analysis of first row transition metals, oxides and hydroxides. *Journal of Physics: Conference Series* **100**, 012025 (2008).
53. Baltrusaitis, J. *et al.* Generalized molybdenum oxide surface chemical state XPS determination via informed amorphous sample model. *Applied Surface Science* **326**, 151–161 (2015).
54. Castle, J. E. & Asami, K. A more general method for ranking the enrichment of alloying elements in passivation films. *Surface and Interface Analysis* **36**, 220–224 (2004).
55. Björck, M. & Andersson, G. GenX: An extensible X-ray reflectivity refinement program utilizing differential evolution. *Journal of Applied Crystallography* **40**, 1174–1178 (2007).
56. Samin, A. J. & Taylor, C. D. First-principles investigation of surface properties and adsorption of oxygen on Ni-22Cr and the role of molybdenum. *Corrosion Science* **134**, 103–111 (2018).
57. Fritzsche, H. *et al.* Neutron Reflectometry. in *Neutron Scattering and Other Nuclear Techniques for Hydrogen in Materials* 115–158 (Springer, Cham, 2016). doi:10.1007/978-3-319-22792-4_5.
58. Penfold, J. & Thomas, R. K. The application of the specular reflection of neutrons to the study of surfaces and interfaces. *Journal of Physics: Condensed Matter* **2**, 1369–1412 (1990).
59. Parratt, L. G. Surface studies of solids by total reflection of x-rays. *Physical Review* **95**, 359–369 (1954).
60. Zhang, X. & Shoesmith, D. W. Influence of temperature on passive film properties on Ni–Cr–Mo Alloy C-2000. *Corrosion Science* **76**, 424–431 (2013).
61. Zhang, X., Qin, Z., Zagidulin, D., Noël, J. J. & Shoesmith, D. W. Effect of Oxide Film Properties on the Kinetics of O_2 Reduction on Alloy C-22. *Journal of The Electrochemical Society* **164**, 911–917 (2017).

62. Henderson, J. D., Li, X., Shoesmith, D. W., Noël, J. J. & Ogle, K. Molybdenum surface enrichment and release during transpassive dissolution of Ni-based alloys. *Corrosion Science* **147**, 32–40 (2019).

63. Baran, G. R. Oxide Compounds on Ni-Cr Alloys. *Journal of Dental Research* **63**, 1332–1334 (1984).

64. Unutulmazsoy, Y., Merkle, R., Mannhart, J. & Maier, J. Chemical diffusion coefficient of Ni in undoped and Cr-doped NiO. *Solid State Ionics* **309**, 110–117 (2017).

65. Yu, X. *et al.* In-situ observations of early stage oxidation of Ni-Cr and Ni-Cr-Mo alloys. *Corrosion* **74**, 939–946 (2018).

66. Lutton Cwalina, K., Demarest, C. R., Gerard, A. Y. & Scully, J. R. Revisiting the effects of molybdenum and tungsten alloying on corrosion behavior of nickel-chromium alloys in aqueous corrosion. *Current Opinion in Solid State and Materials Science* **23**, 129–141 (2019).

67. Nielsen, E. & Larsen, P. Nickel, inorganic and soluble salts. *Evaluation of health hazards and proposal of a health-based quality criterion for drinking water. The Danish Environmental Protection Agency, Copenhagen, Denmark* (2013).

Appendix A – The Cation Concentrations Calculation from the XPS Data

$$x_{Ni^{2+}} = \frac{\frac{A_{NiO}^{tot} + A_{Ni(OH)_2}^{tot}}{S_{Ni}}}{\left[\frac{A_{NiO}^{tot} + A_{Ni(OH)_2}^{tot}}{S_{Ni}} + \frac{A_{Cr_2O_3}^{tot} + A_{Cr(OH)_3}^{tot}}{S_{Cr}} + \frac{A_{MoO_2}^{tot} + A_{MoO_3}^{tot}}{S_{Mo}}\right]} \quad \text{Equation A1}$$

$$x_{Cr^{3+}} = \frac{\frac{A_{Cr_2O_3}^{tot} + A_{Cr(OH)_3}^{tot}}{S_{Cr}}}{\left[\frac{A_{NiO}^{tot} + A_{Ni(OH)_2}^{tot}}{S_{Ni}} + \frac{A_{Cr_2O_3}^{tot} + A_{Cr(OH)_3}^{tot}}{S_{Cr}} + \frac{A_{MoO_2}^{tot} + A_{MoO_3}^{tot}}{S_{Mo}}\right]} \quad \text{Equation A2}$$

$$x_{Mo^{4,6+}} = \frac{\frac{A^{tot}_{MoO_2} + A^{tot}_{MoO_3}}{S_{Mo}}}{\left[\frac{A^{tot}_{NiO} + A^{tot}_{Ni(OH)_2}}{S_{Ni}} + \frac{A^{tot}_{Cr_2O_3} + A^{tot}_{Cr(OH)_3}}{S_{Cr}} + \frac{A^{tot}_{MoO_2} + A^{tot}_{MoO_3}}{S_{Mo}}\right]} \quad \text{Equation A3}$$

where χ_{M^+} is the cation fraction of a generic cation, M^+, A^{tot}_{MO} is the integrated XPS peak area for a generic metal oxide/hydroxide, and S_M is the atomic sensitivity factor for different metals given above.

Appendix B – Neutron Reflectometry Experiment

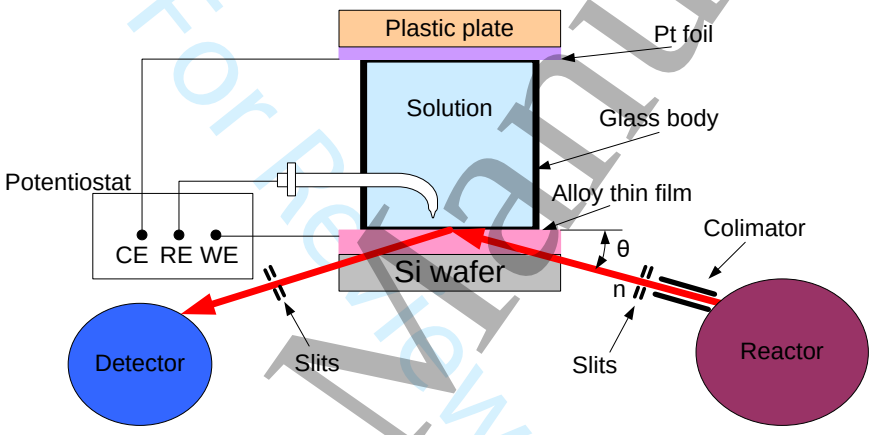

Figure B1. Schematic of the *in situ* neutron reflectometry (NR) experiment at the D3 beamline in the NRU reactor. Collimated neutron beam with a wavelength of 2.37 Å was used for neutron measurements. A custom three-electrode electrochemical cell was employed for chemical and potential condition control.

D3 uses a collimated neutron beam with a wavelength of 2.37 Å. The neutron beam travelled through the Si wafer before it reached the metal/electrolyte interface at a small grazing angle. The intensity of the specular reflected beam was recorded at different grazing angles and the reflectivity curves were plotted as a function of the scattering vector, Q_{beam}, whose magnitude is related to the incident beam angle, θ, and the neutron wavelength, λ, by the following expression[57,58]:

$$Q_{beam} = \frac{4\pi}{\lambda}\sin\theta \quad \text{Equation B1}$$

The thickness, roughness, and scattering length density (SLD) profile of the layers in the thin film sample were obtained by fitting the reflectivity curves to a thin film model using a least square fit algorithm which includes a recursion algorithm developed by Parratt[55,57–59].

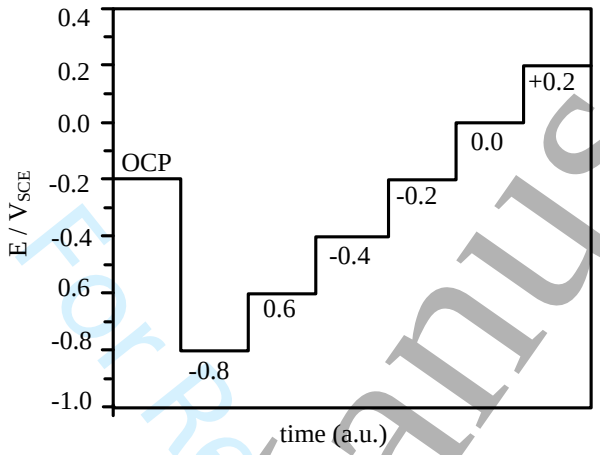

Figure B2. A schematic of the potential steps during *in situ* neutron reflectometry experiments.

Appendix C – XPS analysis of the films formed on Ni-22Cr and Ni-22Cr-6Mo in both the acidic and alkaline environments during the passivation

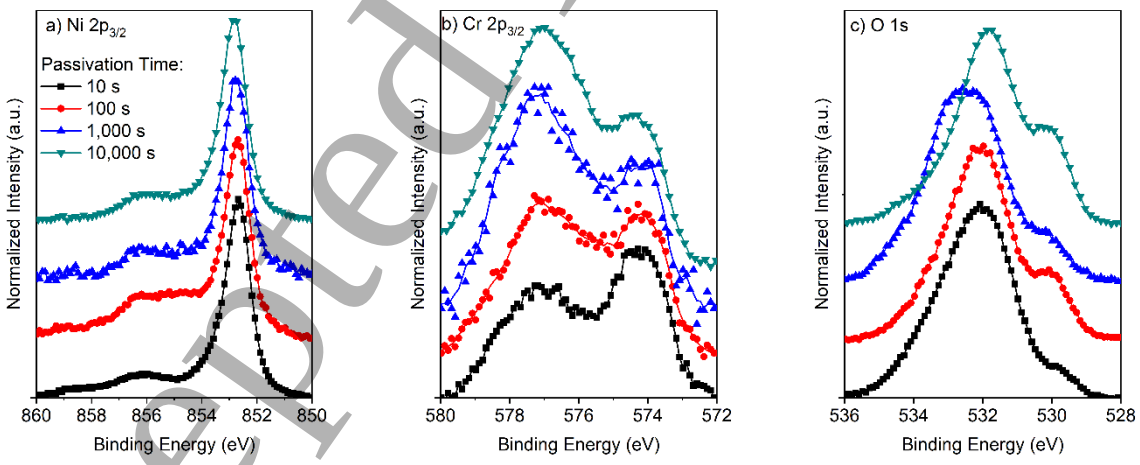

Figure C1. a) Ni $2p_{3/2}$, b) Cr $2p_{3/2}$, and c) O 1s peaks normalized to the metal peaks for Ni-22Cr alloy passivated at +0.2 V_{SCE} for various times up to 10 ks in 0.1 M Na_2SO_4 pH 4.

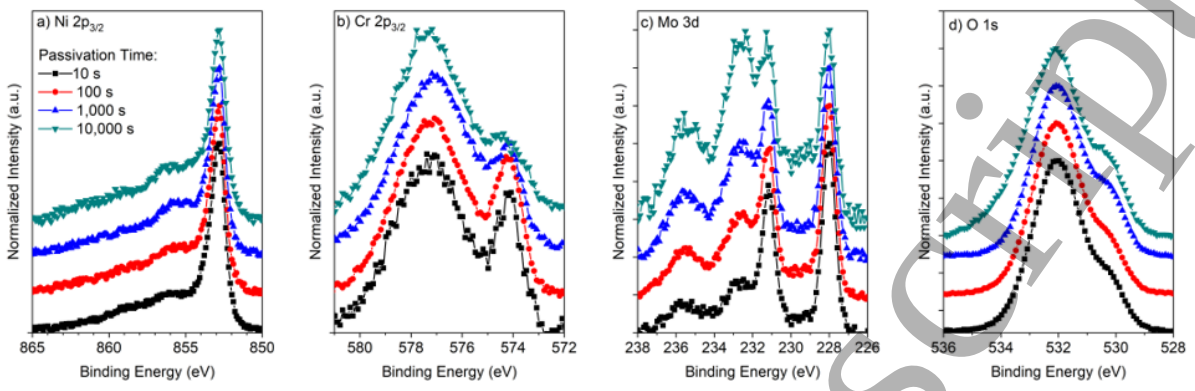

Figure C2. a) Ni $2p_{3/2}$, b) Cr $2p_{3/2}$, c) Mo 3d, and d) O 1s peaks normalized to the metal peaks for Ni-22Cr-6Mo alloy passivated at +0.2 V_{SCE} for various times up to 10 ks in 0.1 M Na_2SO_4 pH 4.

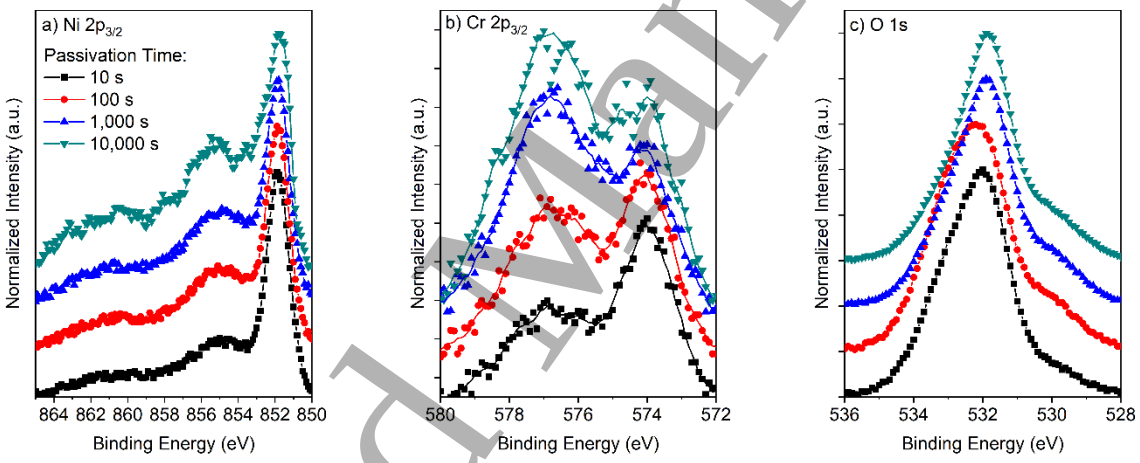

Figure C3. a) Ni $2p_{3/2}$, b) Cr $2p_{3/2}$, and c) O 1s peaks normalized to the metal peaks for Ni-22Cr alloy passivated at +0.2 V_{SCE} for various times up to 10 ks in 0.1 M Na_2SO_4 pH 10.

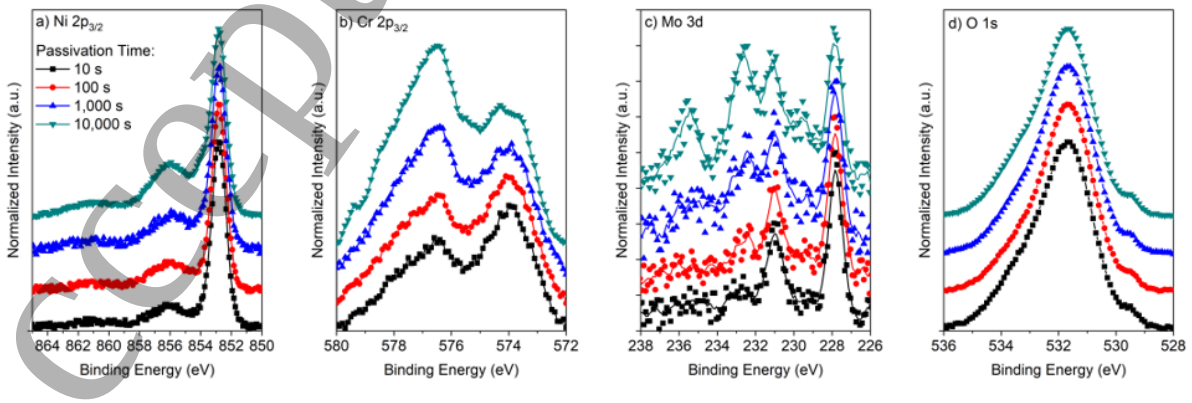

Figure C4. a) Ni $2p_{3/2}$, b) Cr $2p_{3/2}$, c) Mo 3d, and d) O 1s peaks normalized to the metal peaks for Ni-22Cr-6Mo alloy passivated at +0.2 V_{SCE} for various times up to 10 ks in 0.1 M Na_2SO_4 pH 10.

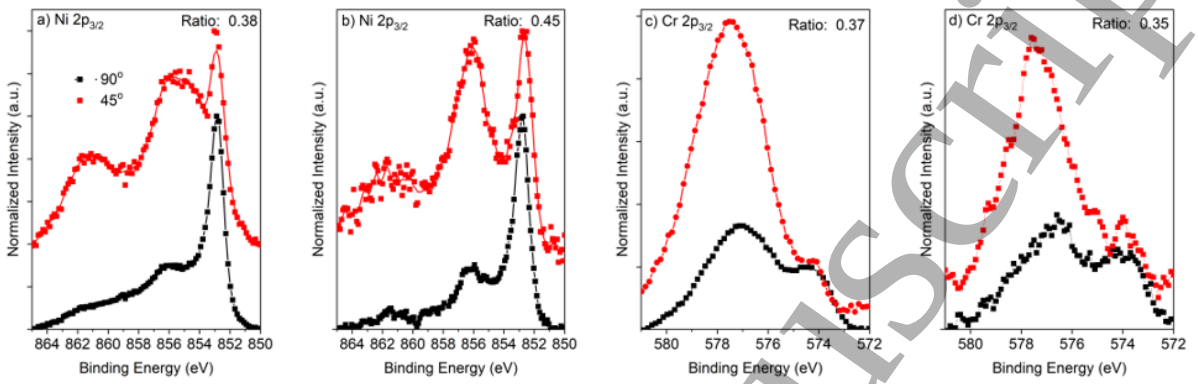

Figure C5. a,b) Ni $2p_{3/2}$ and c,d) Cr $2p_{3/2}$ angle-resolved XPS spectras which were normalized to the metal peaks for Ni-22Cr alloy passivated at +0.2 V_{SCE} for various times up to 10 ks in 0.1 M Na_2SO_4 a,c) pH 4 and b,d) pH 10. The ratio of the oxide areas for each angle measurement is included for reference.

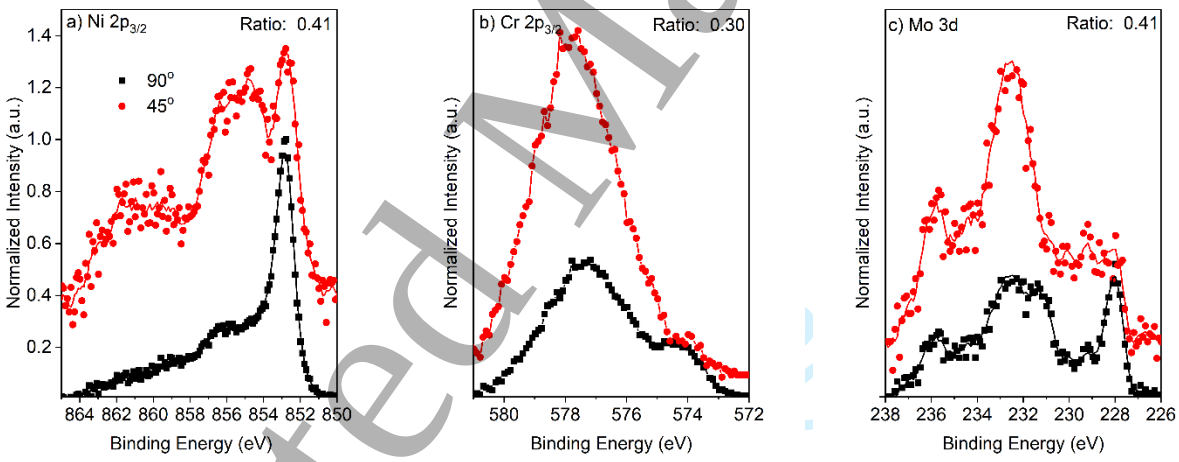

Figure C6. a) Ni $2p_{3/2}$, b) Cr $2p_{3/2}$, and c) Mo 3d angle-resolved XPS spectras which were normalized to the metal peaks for Ni-22Cr-6Mo alloy passivated at +0.2 V_{SCE} for various times up to 10 ks in 0.1 M Na_2SO_4 pH 4. The ratio of the oxide areas for each angle measurement is included for reference.

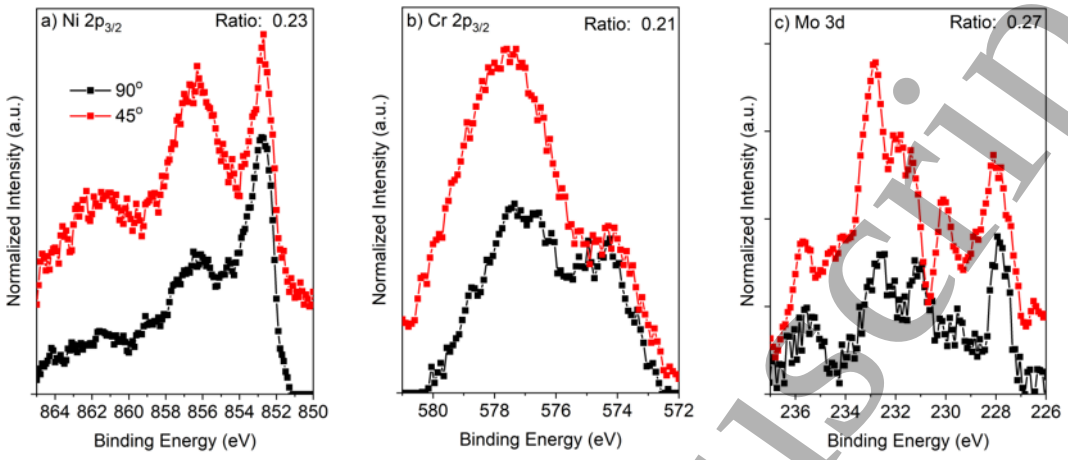

Figure C7. a) Ni $2p_{3/2}$, b) Cr $_{2p3/2}$, and c) Mo 3d angle-resolved XPS spectras which were normalized to the metal peaks for Ni-22Cr-6Mo alloy passivated at +0.2 V_{SCE} for various times up to 10 ks in 0.1 M Na_2SO_4 pH 10. The ratio of the oxide areas for each angle measurement is included for reference.

Figures

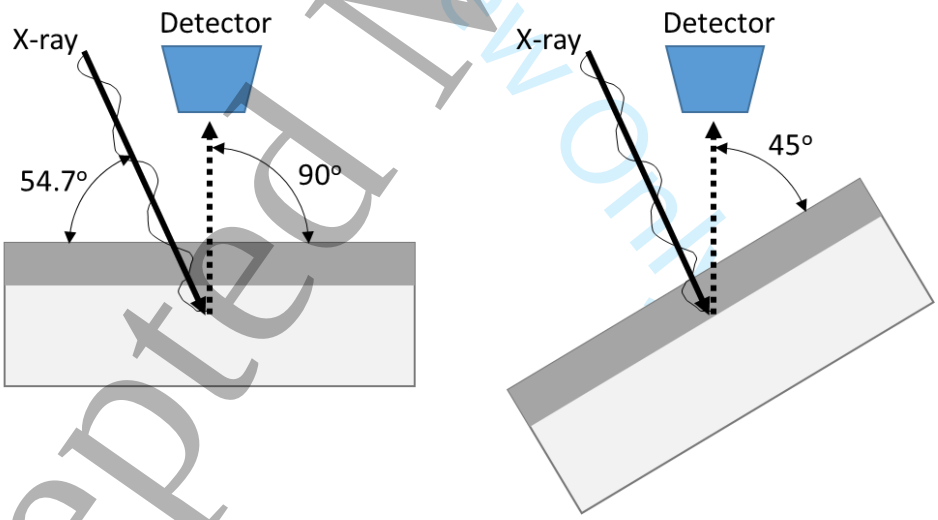

Figure 1. Schematic of the angle-resolved XPS set-up and effect of sample tilting on the probe depth.

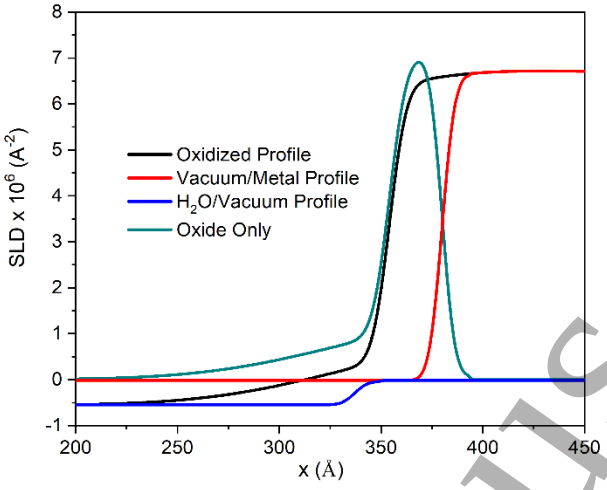

Figure 2. Sample profile subtraction for passivated Ni-22Cr-6Mo, wt%, where SLD profiles for the unoxidized metal and the H_2O were subtracted from the experimental data in order to isolate the profile for the passive film. The same analysis method was applied for all alloys and environments.

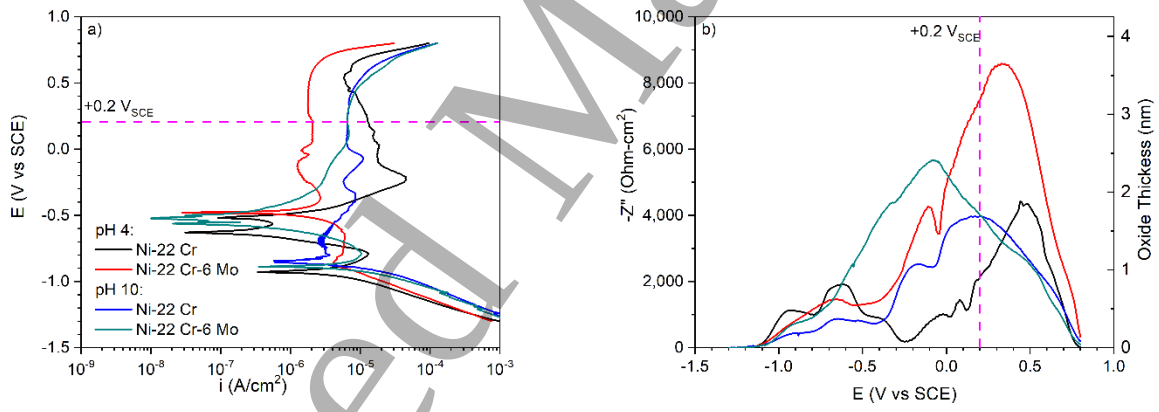

Figure 3. (a) DC current and (b) AC impedance variations during upward potentiodynamic polarization of Ni-22Cr and Ni-22Cr-6Mo alloys in deaerated 0.1 M Na_2SO_4 at pH 4 and 10 with the potential used in this study (+0.2 V_{SCE}) indicated by the dotted lines.

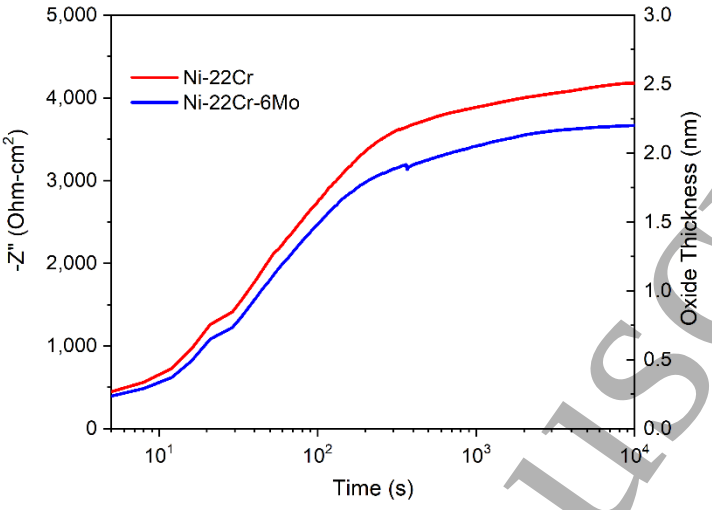

Figure 4. Measured increase in $-Z''$ at 1 Hz during passivation of various Ni-based alloys at +0.2 V_{SCE} in deaerated 0.1 M Na_2SO_4 pH 4 solution for 10 ks with a subsequent full EIS spectrum obtained and fitted in order to compare l_{ox} for each method at the end of the passivation.

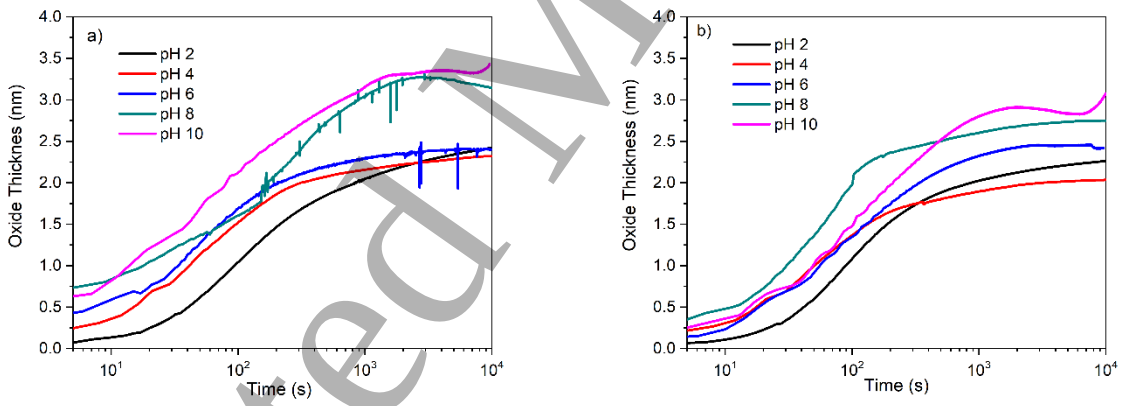

Figure 5. Influence of electrolyte pH on the measured film thickness, l_{ox}, computed using Equation 1 for (a) Ni-22Cr alloy (b) Ni-22Cr-6Mo in 0.1 M Na_2SO_4 solutions.

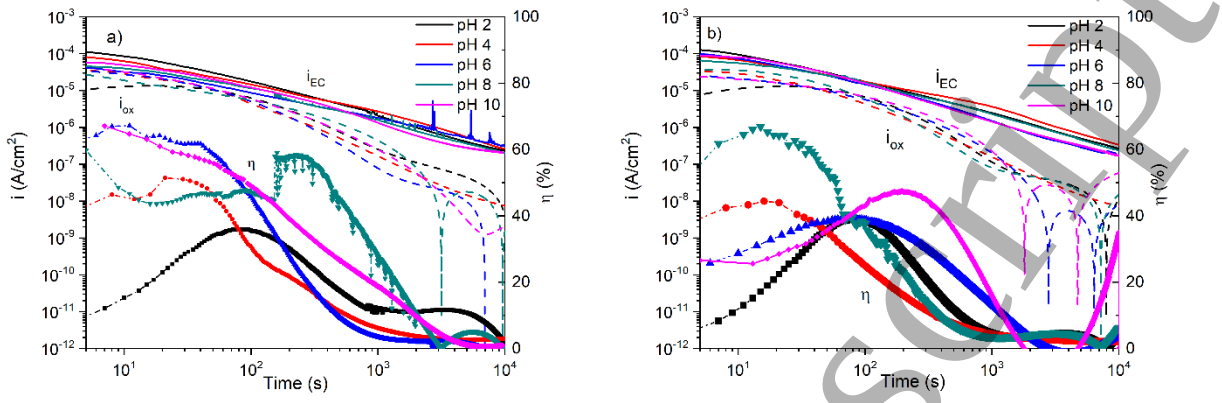

Figure 6. Influence of electrolyte pH on the measured i_{EC} and i_{ox} computed using the SF-EIS results in Figure 5 and Equation 3, and the current efficiency, η, computed using Equation 4 for the (a) Ni-22Cr alloy and, (b) Ni-22Cr-6Mo in 0.1 M Na_2SO_4 solutions.

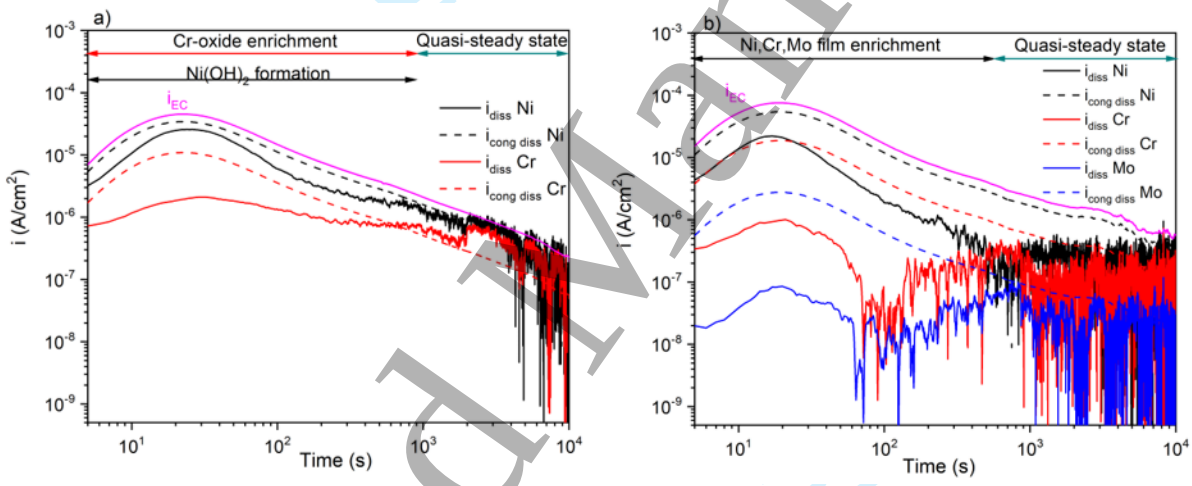

Figure 7. Experimentally determined i_{EC} and experimental i_{diss} AESEC current densities for cation emission versus total element specific current densities for congruent dissolution from the alloys (a) Ni-22Cr and, (b) Ni-22Cr-6Mo held at +0.2 V_{SCE} in 0.1 M Na_2SO_4 pH 4 solution.

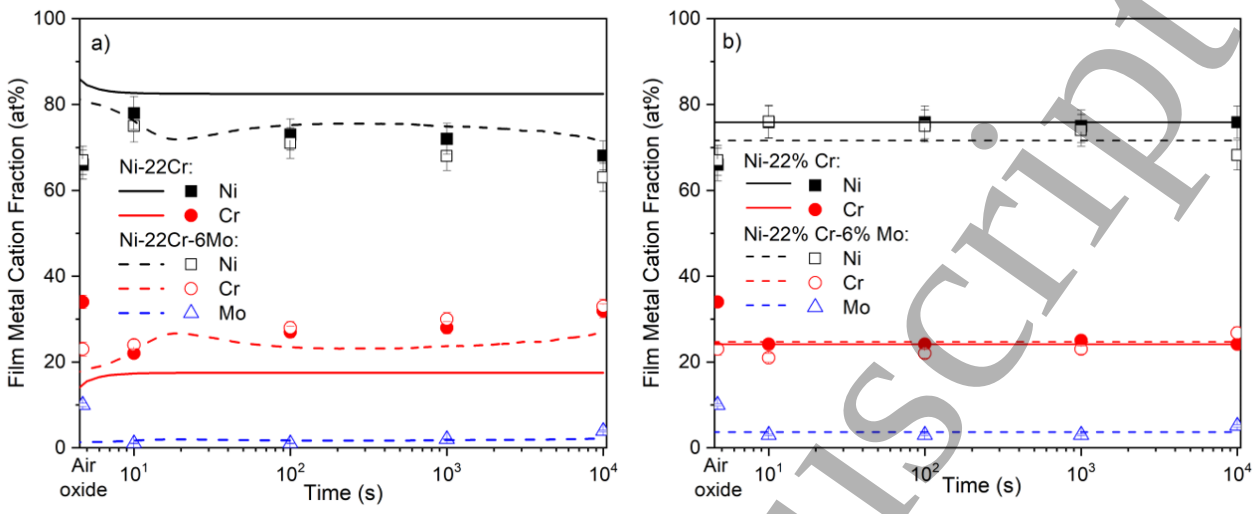

Figure 8. Relative accumulation of metal cations in the passive films during growth at +0.2 V_{SCE} according to AESEC (lines) and XPS (symbols) measurements on the Ni-22Cr and Ni-22Cr-6Mo alloys in 0.1 M Na_2SO_4 (a) pH 4 and, (b) pH 10 solution. Native (air-oxide) composition according to XPS marked at 0 time (symbols).

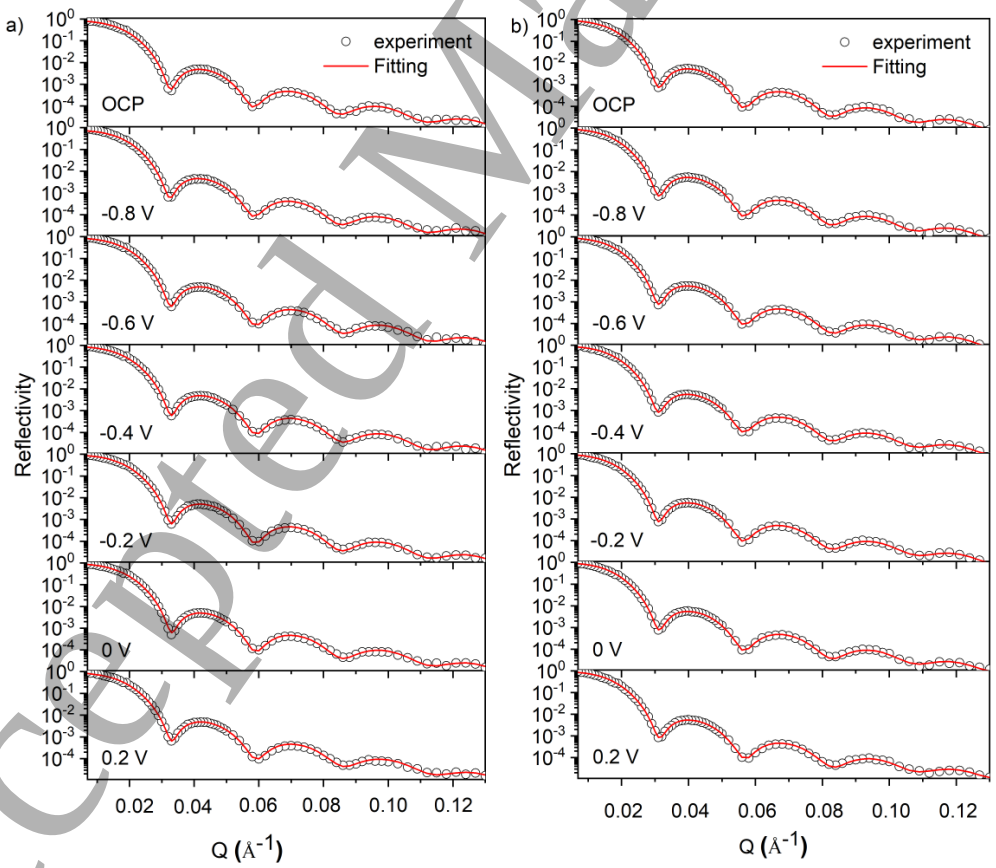

Figure 9. Measured reflectivity curves for a) Ni-20Cr and b) Ni-20Cr-10Mo films oxidized in 0.1 M Na_2SO_4 pH 4 solution at various potential steps (Figure B2, Appendix B). The NR

measurements started 1 hr after the applied potential was switched to the set value and each measurement took approximately 90 minutes to complete

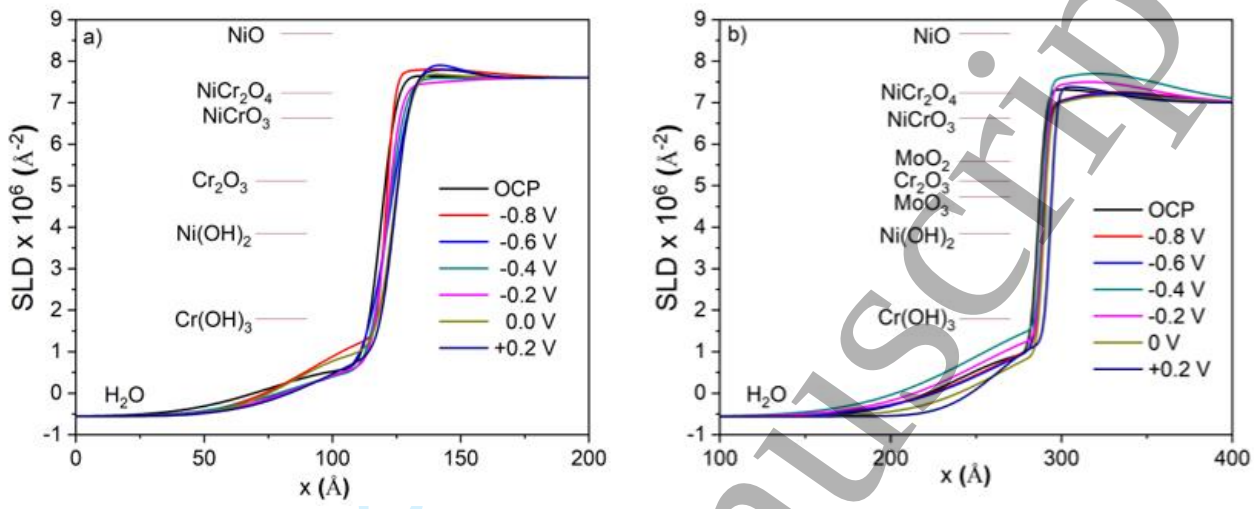

Figure 10. Full SLD profiles for a) the Ni-20Cr film and b) the Ni-20Cr-10Mo film oxidized in 0.1 M Na_2SO_4 pH 4 solution at various potential steps. The theoretical SLD values for differrent materials are indicated by horizontal lines.

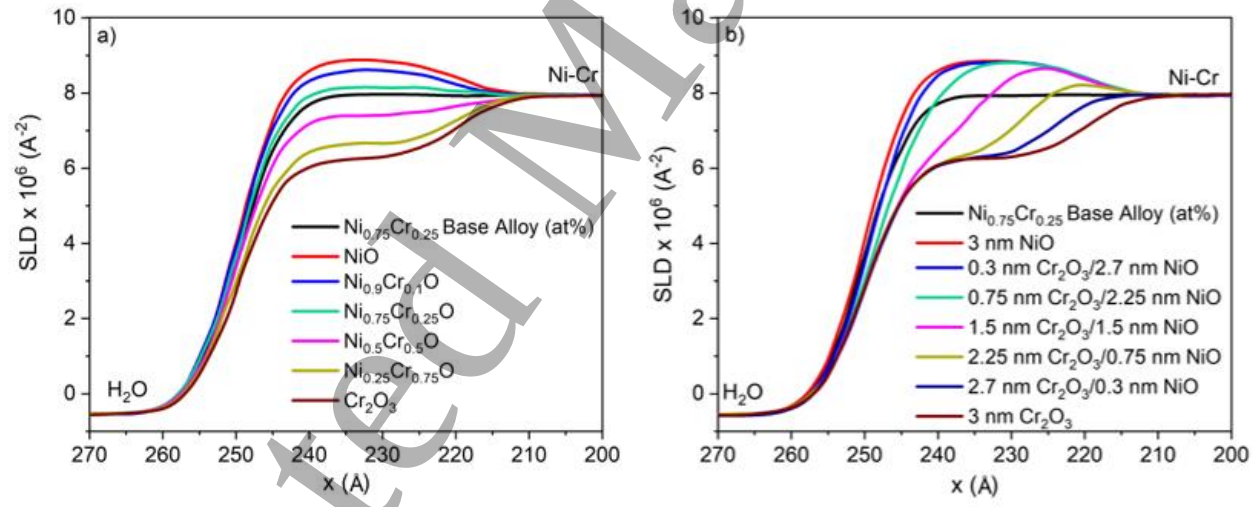

Figure 11. Simulated SLD profiles for a) a non-stoichiometric oxide, $Ni_{1-x}Cr_xO$, containing varying % Cr^{3+} and b) a bilayer oxide comprised of Cr_2O_3 and NiO with varying thickness of each conformal layer. An interfacial roughness of 5 Å was used to replicate the experimental parameter.

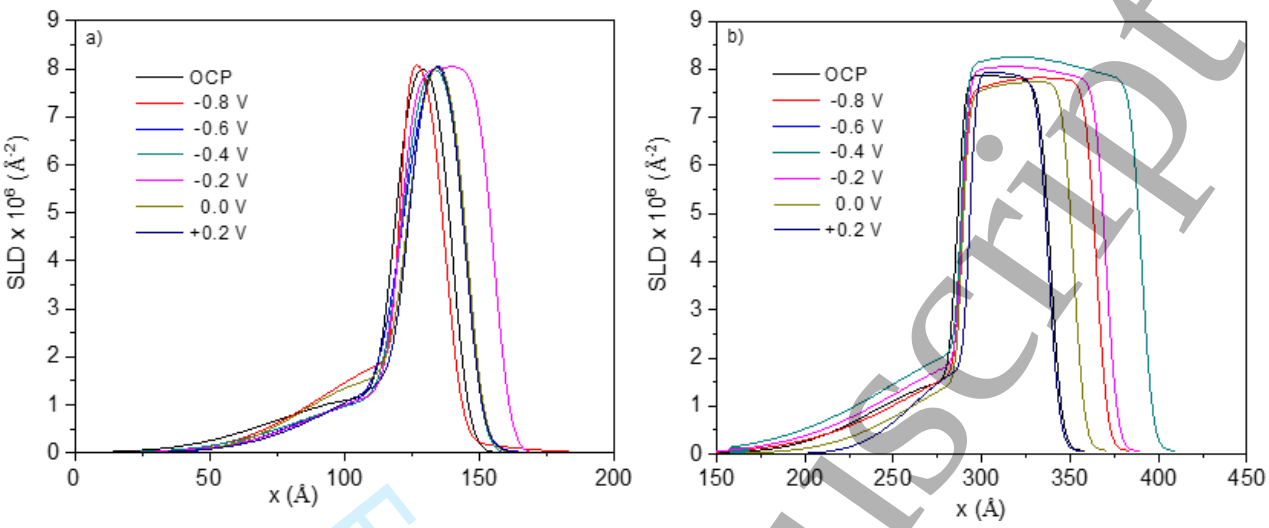

Figure 12. Analysis of the NR profiles given in Figure 10 where a sample profile for the base metal exposed to water on a SiO_2 substrate was simulated and subtracted from the overall reflectometry curve in order to obtain that of just the passive film for a) Ni-20Cr alloy and b) Ni-20Cr-10Mo alloy in 0.1 M Na_2SO_4 pH 4 where the peak SLD correlates to the Cr^{3+} cation fraction and the approximate l_{ox} is indicated by the peak width

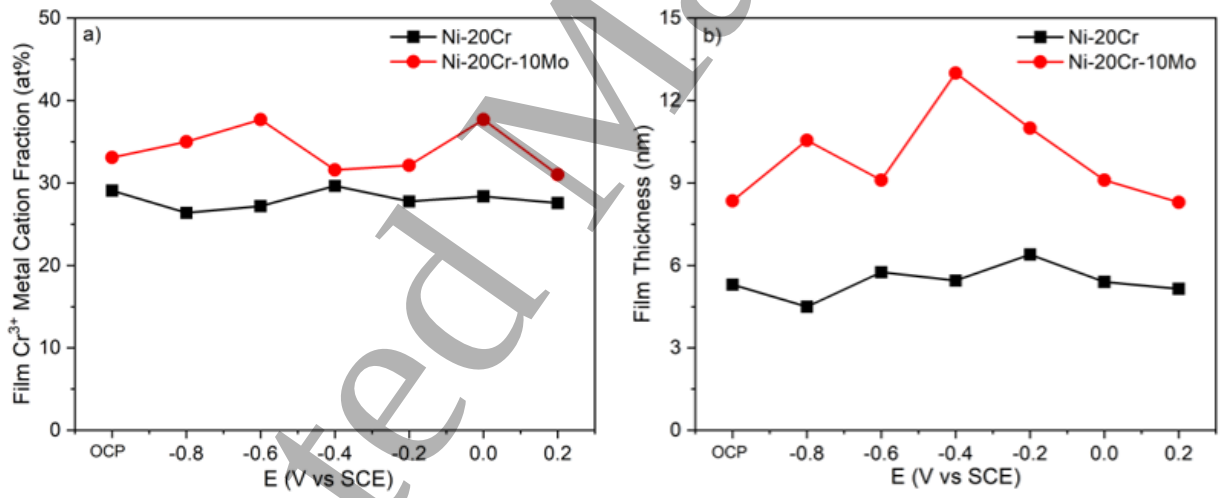

Figure 13. (a) Metal cation fraction and (b) passive film thickness computed from the peak SLD in Figure 12 for Ni-20Cr and Ni-20Cr-10Mo alloys in 0.1 M Na_2SO_4 pH 4 oxidized at varying potentials.

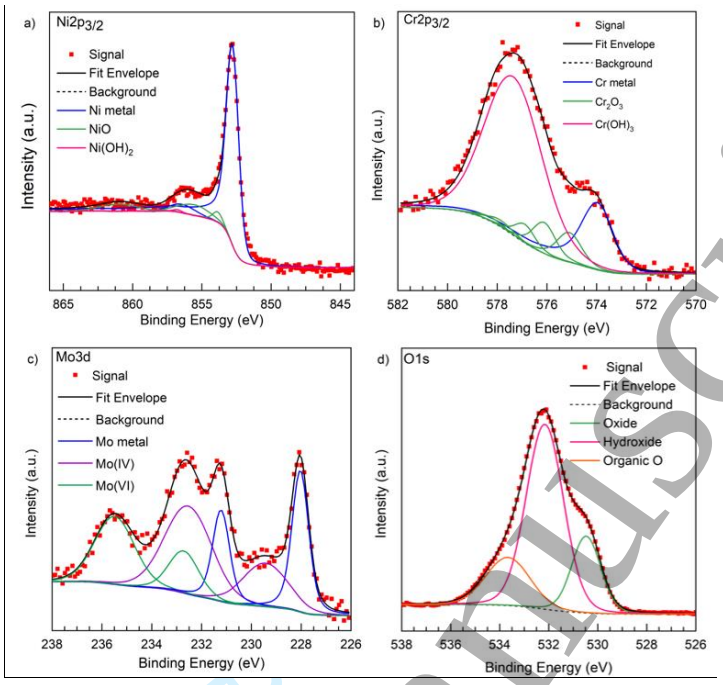

Figure 14. Focused, deconvoluted XPS spectra for a) Ni $2p_{3/2}$, b) Cr $3p_{3/2}$, c) Mo 3d, and d) O 1s bands collected on Ni-22Cr-6Mo alloy passivated at +0.2 V_{SCE} for 10,000 s in 0.1 M Na_2SO_4 pH 4 where the solid black and magenta lines indicate the Shirley background and overall fit to the spectra, respectively.

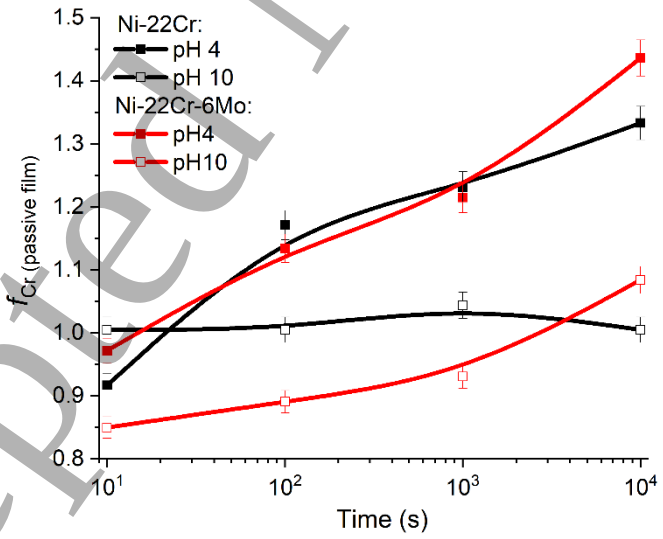

Figure 15. Passive film Cr(III) enrichment/depletion factor $f_{Cr(III)}$ calculatetd by using Equation 13 for Ni-22Cr and Ni-22Cr-6Mo alloys following 10s to 10 ks of potentiostatic passivation at +0.2 V_{SCE} in 0.1 M Na_2SO_4 at pH 4 and 10

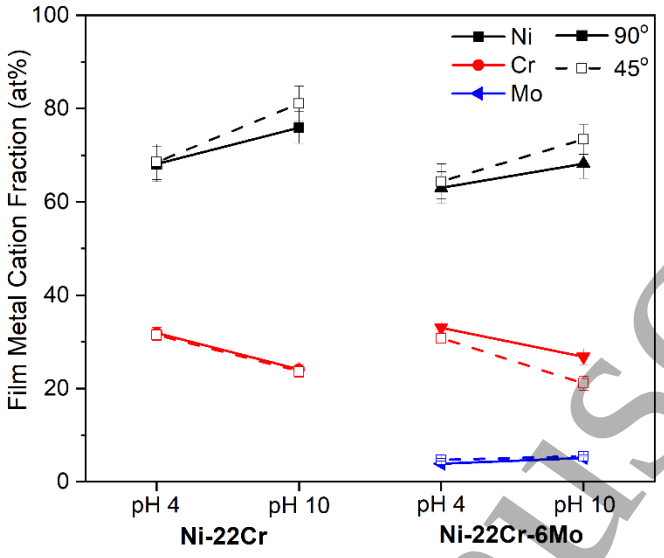

Figure 16. Film cation fraction according to angle-resolved XPS measurements at 90° and 45° on Ni-22Cr and Ni-22Cr-6Mo alloys surfaces following 10 ks of potentiostatic passivation at +0.2 V_{SCE} in 0.1 M Na_2SO_4 at pH 4 and 10.

Table 1. Cation and elemental fractions detected by XPS after 10 min of cathodic reduction at -1.3VSCE in 0.1 M Na2SO4 pH 4 and pH 10 N_2(g) deaerated solution

Alloy	Take-off Angle	Passive Film Cation Fraction			Metal/Film Interface Elemental Fraction		
		Ni	Cr	Mo	Ni	Cr	Mo
Ni-22Cr (pH 4)	90°	0.44	0.56	–	0.78	0.22	–
	45°	0.29	0.71	–	0.81	0.19	–
Ni-22Cr (pH 10)	90°	0.15	0.85	–	0.78	0.22	–
	45°	0.11	0.89	–	0.86	0.14	–
Ni-22Cr-6Mo (pH 4)	90°	0.32	0.57	0.11	0.78	0.17	0.04
	45°	0.28	0.58	0.14	0.81	0.14	0.05
Ni-22Cr-6Mo (pH 10)	90°	0.73	0.18	0.09	0.61	0.25	0.14
	45°	0.69	0.15	0.15	0.58	0.21	0.21